

Stellar masses and star formation histories for 10^5 galaxies from the Sloan Digital Sky Survey

Guinevere Kauffmann,^{1*} Timothy M. Heckman,² Simon D. M. White,¹ Stéphane Charlot,^{1,3} Christy Tremonti,² Jarle Brinchmann,¹ Gustavo Bruzual,⁴ Eric W. Peng,² Mark Seibert,² Mariangela Bernardi,⁵ Michael Blanton,⁶ Jon Brinkmann,⁷ Francisco Castander,⁸ Istvan Csábai,^{9,2} Masataka Fukugita,¹⁰ Zeljko Ivezic,¹¹ Jeffrey A. Munn,¹² Robert C. Nichol,¹³ Nikhil Padmanabhan,¹⁴ Aniruddha R. Thakar,² David H. Weinberg¹⁵ and Donald York⁵

¹Max-Planck Institut für Astrophysik, D-85748 Garching, Germany

²Department of Physics and Astronomy, Johns Hopkins University, Baltimore, MD 21218, USA

³Institut d'Astrophysique du CNRS, 98 bis Boulevard Arago, F-75014 Paris, France

⁴(AE) Centro de Investigaciones de Astronomía, Merida, Venezuela

⁵Department of Astronomy, University of Chicago, 5640 South Ellis Ave, Chicago, IL 60637, USA

⁶Department of Physics, New York University, 4 Washington Place, New York, NY 10003, USA

⁷Apache Point Observatory, PO Box 59, Sunspot, NM 88349, USA

⁸Department of Physics, Yale University, PO Box 208121, New Haven, CT 06520, USA

⁹Department of Physics, Eotvos Lorand University, P.f. 32, H-1518 Budapest, Hungary

¹⁰Institute for Cosmic Ray Research, University of Tokyo, Chiba 277-8582, Japan

¹¹Princeton University Observatory, Peyton Hall, Princeton NJ 08544-1001, USA

¹²US Naval Observatory, Flagstaff Station, PO Box 1149, Flagstaff, AZ 86002, USA

¹³Department of Physics, Carnegie Mellon University, 5000 Forbes Ave, Pittsburgh, PA 15232, USA

¹⁴Department of Physics, Princeton University, Princeton NJ 08544, USA

¹⁵Department of Astronomy, Ohio State University, 140 West 18th Avenue, Columbus, OH 43210, USA

Accepted 2002 November 22. Received 2002 October 30; in original form 2002 April 8

ABSTRACT

We develop a new method to constrain the star formation histories, dust attenuation and stellar masses of galaxies. It is based on two stellar absorption-line indices, the 4000-Å break strength and the Balmer absorption-line index $H\delta_A$. Together, these indices allow us to constrain the mean stellar ages of galaxies and the fractional stellar mass formed in bursts over the past few Gyr. A comparison with broad-band photometry then yields estimates of dust attenuation and of stellar mass. We generate a large library of Monte Carlo realizations of different star formation histories, including starbursts of varying strength and a range of metallicities. We use this library to generate median likelihood estimates of burst mass fractions, dust attenuation strengths, stellar masses and stellar mass-to-light ratios for a sample of 122 808 galaxies drawn from the Sloan Digital Sky Survey. The typical 95 per cent confidence range in our estimated stellar masses is ± 40 per cent. We study how the stellar mass-to-light ratios of galaxies vary as a function of absolute magnitude, concentration index and photometric passband and how dust attenuation varies as a function of absolute magnitude and 4000-Å break strength. We also calculate how the total stellar mass of the present Universe is distributed over galaxies as a function of their mass, size, concentration, colour, burst mass fraction and surface mass density. We find that most of the stellar mass in the local Universe resides in galaxies that have, to within a factor of approximately 2, stellar masses $\sim 5 \times 10^{10} M_\odot$, half-light radii ~ 3 kpc and half-light surface mass densities $\sim 10^9 M_\odot \text{ kpc}^{-2}$. The distribution of $D_n(4000)$ is strongly bimodal, showing a clear division between galaxies dominated by old stellar populations and galaxies with more recent star formation.

Key words: galaxies: evolution – galaxies: formation – galaxies: stellar content.

*E-mail: gamk@mpa-garching.mpg.de

1 INTRODUCTION

The masses of galaxies are traditionally estimated by dynamical methods from the kinematics of their stars and gas. Ever since extended H I rotation curves were first measured for spirals, it has been clear that the implied masses include not only the observed material, but also substantial amounts of dark matter. Indeed, it is now believed that most galaxies are surrounded by dark haloes that extend to many times their optical radii and contain an order of magnitude more mass than the visible components. The properties of these haloes can be inferred directly from tracers at large radii such as X-ray-emitting atmospheres, systems of satellite galaxies, or weak gravitational distortion of background galaxy images. In practice, gaseous atmospheres are visible only around some bright elliptical galaxies, while the other two techniques are too noisy to apply to individual galaxies; they are used to obtain average halo properties for stacked samples of similar galaxies (Zaritsky et al. 1993; McKay et al. 2002).

In order to understand how galaxies formed, we would like to map the relationship between the properties of the observed baryonic components of galaxies and those of their dark haloes. This mapping should yield information concerning how the baryons cooled, condensed and turned into stars as the halo–galaxy systems were assembled, and should clarify the complex physical processes that regulated the efficiency and timing of galaxy formation.

Most studies of the halo–galaxy relation have used luminosity as a surrogate for total baryon content, and a kinematic measure – peak rotation velocity, stellar velocity dispersion, X-ray atmosphere temperature – as a surrogate for halo mass. Both surrogates are far from ideal. Kinematic measures are strongly affected by the visible components of the galaxy and so have an uncertain relation to halo mass; only satellite and weak-lensing studies can reliably estimate total halo masses, albeit as an average over all galaxies in a chosen class. Galaxy luminosity may not correlate well with stellar mass (the dominant baryonic component in all but a subset of the smallest systems). There are strong dependences on the fraction of young stars in the galaxy and on its dust content. Thus a technique to correct for attenuation by dust and to estimate the mass-to-light ratio of the underlying stellar population is needed to estimate the stellar mass of a galaxy.

It is well known that luminosities are less affected by stellar population variations in the near-infrared than in the optical range, and that extinction corrections are also smaller at longer wavelengths. Recently, Verheijen (2001) studied the *B*-, *R*-, *I*- and *K'*-band Tully–Fisher relations of a volume-limited sample of 49 spiral galaxies in the Ursa Major Cluster. He showed that the *K'*-band relation exhibited the tightest correlation with rotation velocity, suggesting that the stellar masses of galaxies are linked closely with the masses of the dark matter haloes in which they formed. The larger scatter in the shorter-wavelength passbands was attributed to variations in star formation history and dust extinction between different galaxies in the sample.

Although near-infrared luminosities are less dependent on star formation history than optical luminosities, they nevertheless exhibit some sensitivity to stellar age. Bell & De Jong (2001) estimate that the near-infrared mass-to-light ratios of local spirals can vary by as much as a factor of 2 and propose a correction based on the optical colours of the galaxies. Brinchmann & Ellis (2000) also used colour-based methods to transform the near-infrared magnitudes of a sample of intermediate redshift galaxies into stellar masses. In both analyses, it was assumed that the star formation histories of galaxies could be described by simple exponential laws. If galaxies formed

a major (>10 per cent) fraction of their stars in recent bursts, it was shown that this would introduce substantial errors into the estimated mass-to-light ratios.

In this paper, we make use of spectral indicators as diagnostics of the past star formation histories of galaxies. In particular, two spectral features, the 4000-Å break and the H δ absorption line, provide important information concerning the ages of the stellar populations in galaxies and are able to distinguish recent star formation histories dominated by bursts from those that are more continuous. We develop a method based on these two indicators and on broad-band photometry that allows us to derive maximum-likelihood estimates of the stellar mass of a galaxy, the attenuation of its starlight by dust, and the fraction of its stars formed in recent bursts. We apply our method to a sample of $\sim 120\,000$ galaxies drawn from the Sloan Digital Sky Survey and show how the derived stellar mass-to-light ratios of galaxies in four Sloan bandpasses (*g*, *r*, *i* and *z*; Fukugita et al. 1996) depend both on galaxy luminosity and on structural parameters such as the concentration index. We also compute the fraction of the total stellar mass in the Universe in galaxies of different masses, sizes, colours and concentrations. The dependence of galaxy properties on stellar mass is addressed in a separate paper (Kauffmann et al. 2003, Paper II).

2 DESCRIPTION OF THE OBSERVATIONAL SAMPLE AND SPECTRAL REDUCTIONS

The sample of galaxies analysed in this paper is drawn from the Sloan Digital Sky Survey. This survey will obtain *u*, *g*, *r*, *i* and *z* photometry of almost a quarter of the sky and spectra of at least 700 000 objects. The survey goals and procedures are outlined in York et al. (2000) and a description of the data products and pipelines is given in Stoughton et al. (2002).

Our sample of galaxies is drawn from all available spectroscopic observations in the SDSS Data Release One (DR1). We have included all objects spectroscopically classified as galaxies with Petrosian *r*-band magnitudes in the range $14.5 < r < 17.77$ after correction for foreground galactic extinction using the reddening maps of Schlegel, Finkbeiner & Davis (1998). This is equivalent to the ‘main’ galaxy sample designed for large-scale structure studies. Our sample contains a total of 122 808 galaxies. More details concerning the SDSS photometric system may be found in Fukugita et al. (1996) and Smith et al. (2002). Information relating to the SDSS camera and photometric monitoring system can be found in Gunn et al. (1998) and Hogg et al. (2001). Details of the spectroscopic target selection of galaxies are given in Strauss et al. (2002).

The spectra were reduced using version v4.9.5 of the SPECTRO2D pipeline. The processed spectra are wavelength- and flux-calibrated. The spectral indicators (primarily the 4000-Å break and the H δ_A index) and the emission lines (the equivalent widths and fluxes of H α and H β) that are discussed in this paper are calculated using a special-purpose code described in detail in Tremonti et al. (in preparation). Here we provide a brief summary of the main features of the code.

Galaxies display a very rich stellar absorption-line spectrum, which encodes much information concerning their stellar populations, but complicates measurements of nebular emission lines. In most early-type galaxies, the [O II], [O III] and H α emission lines are similar in strength to fluctuations produced by the many superposed stellar absorption features. Although late-type galaxies tend to have stronger emission lines and spectra dominated by hotter, more featureless stars, stellar Balmer absorption can still be substantial (2–4 Å at H β).

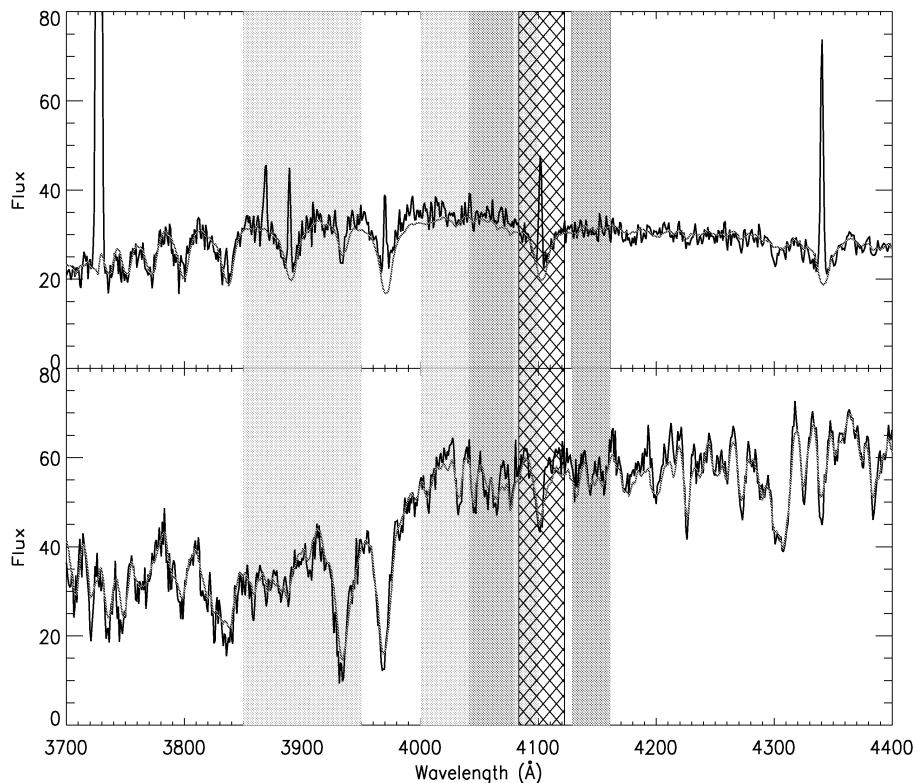


Figure 1. SDSS spectra of a late-type galaxy (top) and an early-type galaxy (bottom) are plotted over the interval 3700–4400 Å in the restframe. The red line shows our best-fitting BC2003 model spectrum. The light grey-shaded regions indicate the bandpasses over which the $D_n(4000)$ index is measured. The dark grey regions show the pseudocontinua for the $H\delta_A$ index, while the hatched region shows the $H\delta_A$ bandpass.

We therefore perform a careful subtraction of the stellar absorption-line spectrum before measuring the nebular emission lines. This is accomplished by fitting the emission-line-free regions of the spectrum with a model spectrum. The models are based on the new population synthesis code of Bruzual & Charlot (2003, hereafter BC2003), which incorporates high-resolution (3-Å FWHM) stellar libraries. (Salient details of the libraries are discussed further in Section 3.) We have generated a set of 39 template spectra spanning a wide range in age and metallicity. The template spectra are convolved with a Gaussian to match the stellar velocity dispersion of each galaxy and rebinned to the SDSS dispersion ($\Delta \log \lambda = 10^4$). The best-fitting model spectrum is constructed from a non-negative linear combination of the template spectra, with dust attenuation modelled as a $\lambda^{-0.7}$ power law of adjustable amplitude (Charlot & Fall 2000).

In Fig. 1, we plot two representative SDSS galaxy spectra over the wavelength interval 3700–4400 Å (restframe), which includes both the 4000-Å break and the $H\delta$ absorption features that are used extensively in this paper. The upper panel in Fig. 1 shows the spectrum of a star-forming galaxy with strong Balmer emission lines, while the lower panel shows a typical early-type galaxy with strong stellar absorption features. The red lines in Fig. 1 show the best-fitting model to the stellar absorption spectrum over the wavelength interval from 3600 to 6800 Å. We find that in general, the BC2003 models reproduce the main stellar absorption features of galaxies in the SDSS survey extremely well.

A more detailed analysis of the spectral fits will be presented in Tremonti et al. (in preparation). We note that the top panel of Fig. 1 demonstrates that in star-forming galaxies, high-resolution models are *required* in order to separate the Balmer emission lines from

the underlying stellar absorption features in a reliable way. Without these models, the accuracy of the emission-line measurements is compromised by an unknown correction for stellar absorption. Likewise, stellar continuum indices such as $H\delta_A$ will be contaminated by emission lines unless these can be removed.

All magnitudes quoted in this paper are Petrosian magnitudes. For the SDSS, the Petrosian radius is defined as the largest radius at which the local r -band surface brightness is at least one-fifth the mean surface brightness interior to that radius. The Petrosian flux is then the total flux within a circular aperture of twice the Petrosian radius. Details concerning the Petrosian flux measurements are given in Lupton et al. (in preparation) and Strauss et al. (2002). The SDSS Petrosian magnitude detects essentially all the light from galaxies with exponential profiles and more than 80 per cent of the light from galaxies with de Vaucouleurs profiles.

Conversions from apparent magnitude to absolute magnitude depend on cosmology through the distance modulus $DM(z)$ and on galaxy type through the K -correction $K(z)$:

$$M = m - DM(z) - K(z). \quad (1)$$

We assume a Friedmann–Robertson–Walker cosmology with $\Omega = 0.3$, $\Lambda = 0.7$ and $H_0 = 70 \text{ km s}^{-1} \text{ Mpc}^{-1}$. We calculate the K -corrections $K(z)$ for each galaxy using the routines in KCORRECT v1.11 (Blanton et al. 2002a). In order to minimize the errors in this procedure, we K -correct the magnitudes of all galaxies in our sample to $z = 0.1$, which is close to the median redshift of the galaxies in our sample. Blanton et al. have studied the errors in the K -corrections by comparing the magnitudes produced by the KCORRECT routine with broad-band magnitudes synthesized from the galaxy spectra themselves. The conclusion is that r -, i - and z -band magnitudes can

be reconstructed to the level of the photometry (~ 1 per cent). The g - and u -band magnitudes have considerably larger errors (5 and 20 per cent, respectively). We will not consider u -band magnitudes in this paper.

3 SPECTRAL DIAGNOSTICS OF BURSTS

The break occurring at 4000 Å is the strongest discontinuity in the optical spectrum of a galaxy and arises because of the accumulation of a large number of spectral lines in a narrow wavelength region. The main contribution to the opacity comes from ionized metals. In hot stars, the elements are multiply ionized and the opacity decreases, so the 4000-Å break will be small for young stellar populations and large for old, metal-rich galaxies. A break index $D(4000)$ was defined by Bruzual (1983) as the ratio of the average flux density F_ν in the bands 4050–4250 and 3750–3950 Å. A definition using narrower continuum bands (3850–3950 and 4000–4100 Å) was recently introduced by Balogh et al. (1999). The principal advantage of the narrow definition is that the index is considerably less sensitive to reddening effects. We will adopt the narrow definition as our standard in this paper and we denote this index as $D_n(4000)$.

Strong H δ absorption lines arise in galaxies that experienced a burst of star formation that ended ~ 0.1 –1 Gyr ago. The peak occurs once hot O and B stars, which have weak intrinsic absorption, have terminated their evolution. The optical light from the galaxies is then dominated by late-B to early-F stars. Worthey & Ottaviani (1997) defined an H δ_A index using a central bandpass bracketed by two pseudo-continuum bandpasses. They parametrized the strength of this feature as a function of stellar effective temperature, gravity and metallicity using the Lick/IDS spectral library (Gorgas et al. 1993). A similar calibration of the 4000-Å break strength has been carried out by Gorgas et al. (1999). Most currently available stellar population synthesis models have very low spectral resolution. The resolution of the Lick/IDS spectral library is 9 Å, a factor of 4 lower than that of the SDSS spectra. The models of Bruzual & Charlot (1993) have a 20-Å spectral resolution, far too low to measure the H δ absorption feature and $D_n(4000)$ index reliably.

High-resolution stellar spectral libraries spanning a wide range in metallicity, spectral type and luminosity class have only recently become available. The STELIB library (Le Borgne et al. 2002) consists of over 250 stars spanning a range of metallicities from 0.05 to 2.5 times solar, a range of spectral types from O5 to M9 and luminosity classes from I to V. The coverage in spectral type is not uniform at all metallicities: hot ($T_{\text{eff}} > 20\,000$ K) stars of sub-solar metallicity are underrepresented, and the library lacks very cool ($T_{\text{eff}} < 3500$ K) stars of all metallicities. The spectra cover the wavelength range from 3500 to 9500 Å with a resolution of 3-Å FWHM and a signal-to-noise (S/N) ratio of ~ 50 . Most of the stars in the library were selected from the catalogue of Cayrel de Strobel et al. (1992), which contains Fe/H determinations obtained from high-resolution spectroscopic observations. The selection of stars was optimized to provide good coverage of the Hertzsprung–Russell diagram. This stellar library has now been incorporated in the latest version of the Bruzual & Charlot (1993) population synthesis code. A full description of the code and of the new stellar library will be presented elsewhere (BC2003). A description of the underlying stellar evolution prescriptions used in these models (stellar evolutionary tracks and their semi-empirical extensions) can be found in Liu, Charlot & Graham (2000).

The evolution of the $D_n(4000)$ and H δ_A indices following an instantaneous burst of star formation is illustrated in Fig. 2. The

left-hand panels show the evolution of the two indices for a solar metallicity single-age stellar population (SSP). In order to assess how much systematic uncertainty there is in the calibration of these two indices, we have compared model predictions using three different empirical stellar libraries: (i) the STELIB library with 3-Å resolution (Le Borgne et al. 2002), (ii) the Pickles (1998) library with 5-Å resolution and (iii) the Jacoby, Hunter & Christian (1984) library with 4.5-Å resolution. Our results show that at fixed metallicity and age, the variations in the behaviour of the indices arising from differences in the input stellar libraries are ~ 0.05 for the $D_n(4000)$ index and ~ 1 Å for H δ_A . For very old stellar populations, the systematic differences are somewhat larger. In the right-hand panels, we compare the evolution of the two indices for SSPs of differing metallicity. Results are shown only for the STELIB library. There are no other high-resolution libraries of stars of non-solar metallicity that span a wide range in wavelength, spectral type and luminosity class, so we are unable to carry out an analysis of systematic effects for non-solar models. As can be seen, the evolution of $D_n(4000)$ does not depend strongly on metallicity until ages of more than 10^9 yr after the burst. The strongest dependence of the H δ_A index on metallicity also occurs at old ages. The calibration in Fig. 2 does not take into account the effects of the velocity dispersion of the stars in galaxies. We tested whether this would make any difference to our index calibrations and we find that the effects on H δ_A and $D_n(4000)$ are negligible. (We note that this is *not* true for all the Lick indices.)

Although the time evolution of the $D_n(4000)$ and H δ_A indices does depend on metallicity, the *locus* of galaxies in the $D_n(4000)$ –H δ_A plane is not as sensitive to metallicity and is a powerful diagnostic of whether galaxies have been forming stars continuously or in bursts over the past 1–2 Gyr. In addition, these two stellar indices are largely insensitive to the dust attenuation effects that complicate the interpretation of broad-band colours. In Fig. 3 we plot H δ_A as a function of $D_n(4000)$ for ‘pure burst’ star formation histories and for continuous star formation histories spanning a large range of formation times t_{form} and exponential star formation time-scales. Results are shown for three different metallicities. As can be seen, the continuous models occupy a narrow band in the $D_n(4000)$ –H δ_A plane. Galaxies with stronger H δ_A absorption strength at a given value of $D_n(4000)$ must have formed some fraction of their stars in a recent burst.

In Fig. 3, we also show the region of the $D_n(4000)$ –H δ_A plane populated by SDSS galaxies. We show the subset of galaxies for which the error in the measured value of H δ_A is less than 0.8 Å and the error in the $D_n(4000)$ index is less than ~ 0.03 . This cut includes $\sim 25\,000$ galaxies or 20 per cent of the total sample. The mean errors on the $D_n(4000)$ and H δ_A indices for the full sample are 0.048 and 1.4 Å, respectively. We have corrected the H δ_A measurements for contamination owing to nebular emission. Because the H δ emission is so much weaker than that at H α or H β , even in the dust-free case, the most robust way to correct for it is to scale directly from the measured H α flux. We use the difference between the observed H α –H β emission-line fluxes and the dust-free case-B recombination value (2.86) to calculate the attenuation of the emission lines. We assume an attenuation law of the form $\tau_\lambda \propto \lambda^{-0.7}$ (Charlot & Fall 2000). It is then straightforward to calculate the emission correction to the H δ_A index. We apply this correction to all galaxies where the H α and H β emission lines are measured with $S/N > 3$. The typical emission correction to H δ_A for late-type galaxies with $D_n(4000) < 1.4$ is around 1 Å. For early-type galaxies, it is smaller. We have also corrected the $D_n(4000)$ index for contamination by the [Ne III] emission line at 3869 Å. This only affects a very small fraction of galaxies – mainly Seyfert IIs. Fig. 3 shows that there is

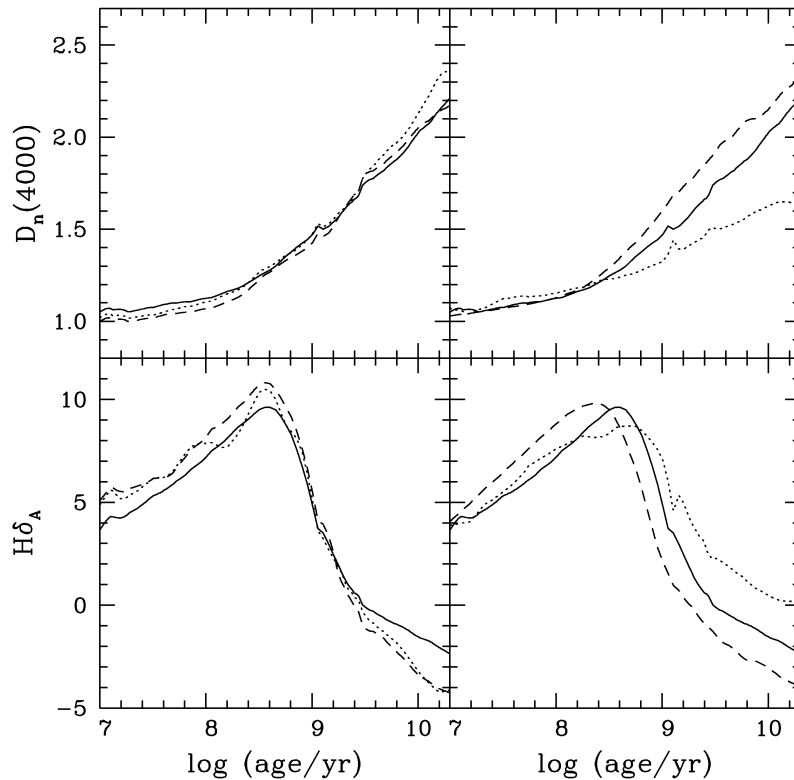


Figure 2. Left: the evolution of $D_n(4000)$ and $H\delta_A$ following an instantaneous, solar-metallicity burst of star formation. Solid lines show results from BC2003+STELIB, the dotted line shows results if the Pickles (1998) library is used, and the dashed line is for the Jacoby et al. (1984) library. Right: the evolution of $D_n(4000)$ and $H\delta_A$ for bursts of different metallicity. The solid line is a solar metallicity model, the dotted line is a 20 per cent solar model and the dashed line as a 2.5 solar model.

good agreement between the area of the $D_n(4000)$ – $H\delta_A$ plane populated by real galaxies and the values predicted by the population synthesis models. We now investigate the effect of different star formation histories on the estimated stellar mass-to-light ratios of our galaxies.

4 A LIBRARY OF STAR FORMATION HISTORIES

We use a Bayesian technique to derive estimates of the stellar mass-to-light ratios, dust attenuation corrections and burst mass fractions for each galaxy in our sample. We also derive associated confidence intervals for each of these parameters. A generalized description of the mathematical basis of our technique is given in Appendix A.

In Bayesian statistics, an initial assumption is made that the data are randomly drawn from a distribution, which is a family of models characterized by a parameter vector \mathbf{P} . One has to specify a prior distribution on the space of all possible \mathbf{P} . This is a probability density distribution that encodes knowledge concerning the relative likelihood of various \mathbf{P} values in the absence of any data. Typically one takes a uniform prior in parameters with a small dynamic range and a uniform prior in the logarithm of parameters with a large dynamic range.

We set up our prior distribution by generating a library of Monte Carlo realizations of different star formation histories. It is important that our library of models span the full range of physically plausible star formation histories, and that it be uniform in the sense that all histories are reasonably represented and no a priori implausible corner of parameter space accounts for a large fraction of the models.

In our library, each star formation history consists of two parts.

(i) An underlying continuous model parametrized by a formation time t_{form} and a star formation time-scale parameter γ . Galaxies form stars according to the law $\text{SFR}(t) \propto \exp[-\gamma t \text{ (Gyr)}]$ from time t_{form} to the present. We take t_{form} to be distributed uniformly over the interval from the big bang to 1.5 Gyr before the present day and γ over the interval 0 to 1. We do not allow star formation rates that increase with time ($\gamma < 0$) because these are very similar to bursts.

(ii) We superimpose random bursts on these continuous models. The amplitude of a burst is parametrized as $A = M_{\text{burst}}/M_{\text{cont}}$, where M_{burst} is the mass of stars formed in the burst and M_{cont} is the total mass of stars formed by the continuous model from time t_{form} to the present. A is distributed logarithmically from 0.03 to 4.0. During the burst, stars form at a constant rate for a time t_{burst} distributed uniformly in the range 3×10^7 – 3×10^8 yr. Bursts occur with equal probability at all times after t_{form} and we have set the probability so that 50 per cent of the galaxies in the library have experienced a burst over the past 2 Gyr. Bursting and continuous models are thus equally represented [recall that our stellar indicators $H\delta_A$ and $D_n(4000)$ are only sensitive to bursts occurring during the past 1–2 Gyr]. In Section 6.2, we explore to what extent altering the mix of continuous and bursty star formation histories changes estimated parameters such as the mass-to-light ratios and burst mass fractions.

We adopt the universal initial mass function (IMF) as parametrized by Kroupa (2001). It is very similar in form to the IMF proposed by Kennicutt (1983). Our models are distributed uniformly in metallicity from 0.25 to 2 times solar. Our final library consists of 32 000 different star formation histories. For each history,

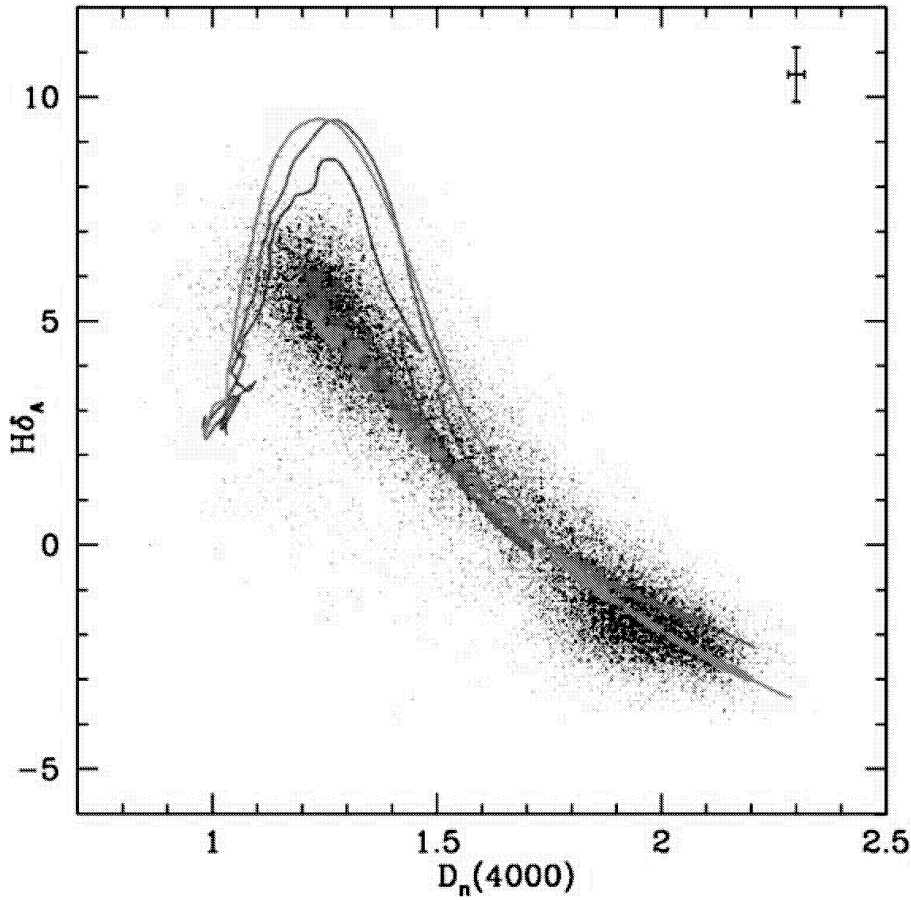


Figure 3. $H\delta_A$ is plotted as a function of $D_n(4000)$ for 20 per cent solar, solar and 2.5 times solar metallicity bursts (blue, red and magenta lines), and for 20 per cent solar, solar and 2.5 solar continuous star formation histories (blue, red and magenta symbols). A subset of the SDSS data points with small errors are plotted as black dots. The typical error bar on the observed indices is shown in the top right-hand corner of the plot.

we store a variety of different parameters, including the predicted values of $D_n(4000)$, $H\delta_A$, the value of the stellar mass-to-light ratio in the z band, the $g-r$ and $r-i$ colours of the stellar populations of the model galaxies, and the fraction of the total stellar mass of the galaxy formed in bursts over the past 2 Gyr (we will denote this parameter as F_{burst}). Fig. 4 illustrates how our model galaxies populate the $D_n(4000)$ – $H\delta_A$ plane. Even though 50 per cent of the galaxies have had a starburst of varying amplitude over the past 2 Gyr, most of the models lie close to the locus of continuous star formation histories. The fact that our models are distributed inhomogeneously in the $D_n(4000)$ – $H\delta_A$ plane has a significant impact on the confidence intervals we derive for our parameters. For example, a galaxy will have a relatively high probability of being scattered from the continuous to the bursting region of the plane by observational errors. It will have a much smaller probability of being scattered the other way around. We will illustrate this in more detail in the next section.

In the left-hand panel of Fig. 5, we divide the $D_n(4000)$ – $H\delta_A$ plane into bins and we have coded each bin with a different symbol to reflect the average z -band mass-to-light ratio of the simulated galaxies that fall into it. As can be seen, the mass-to-light ratio is primarily a sequence in $D_n(4000)$, but at fixed $D_n(4000)$, galaxies with strong $H\delta$ absorption have a higher fraction of young stars and hence have smaller mass-to-light ratios. As well as average values, one can also compute the 1σ dispersion in these parameters as a function of position in the plane. This is shown in the right-hand

panel of Fig. 5 and gives an indication of the accuracy with which mass-to-light ratios could be derived from the models if there were no observational errors and in the absence of dust. As can be seen, the logarithm of the z -band mass-to-light ratio can be determined to better than 0.1 dex for galaxies with $D_n(4000) > 1.6$. For galaxies with $D_n(4000) < 1.6$, $\log(M/L)_z$ is still determined to better than 0.15 dex for all but the very youngest systems.

In Fig. 6, the bins are coded according to the *fraction* of model SFHs with F_{burst} in a given range. Regions where more than 95 per cent of the models in the grid have $F_{\text{burst}} > 0.05$ are indicated using solid and open triangles. If a galaxy has measured indices that lie in this region and the errors are small, then one can say with high confidence that the galaxy has experienced a burst over the past 2 Gyr. In areas coded with solid triangles, 95 per cent of galaxies are currently experiencing or have experienced a burst that began no more than 0.1 Gyr ago. Galaxies in this region may be better termed ‘starburst’ rather than ‘post-starburst’ systems. The areas of the diagram coded with solid squares indicate regions where more than 95 per cent of the models have $F_{\text{burst}} = 0$. If a galaxy lies in this region, one can say with high confidence that a galaxy did *not* form a significant fraction of its stellar population in a burst over the past 2 Gyr. A significant fraction of the diagram is coded with crosses. These regions contain a mix of bursty and continuous models. The values of F_{burst} derived for galaxies in this region will depend strongly on how one chooses the mix of star

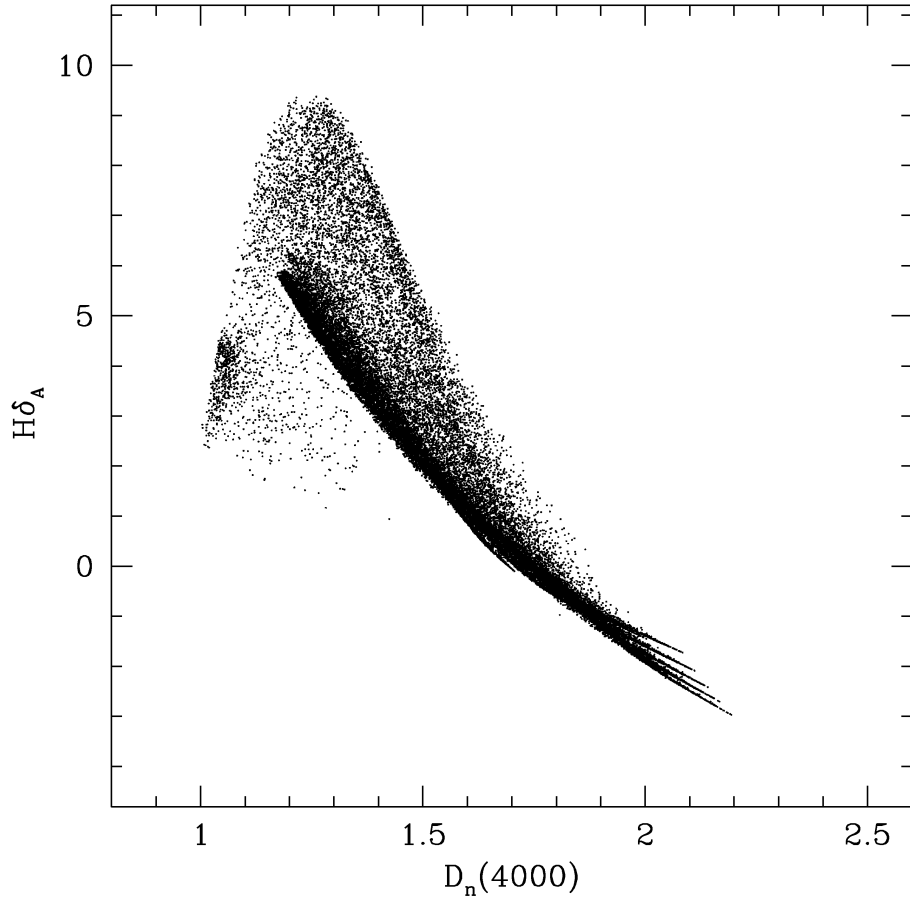


Figure 4. The distribution of galaxies in our model library in the $D_n(4000)$ – $H\delta_A$ plane.

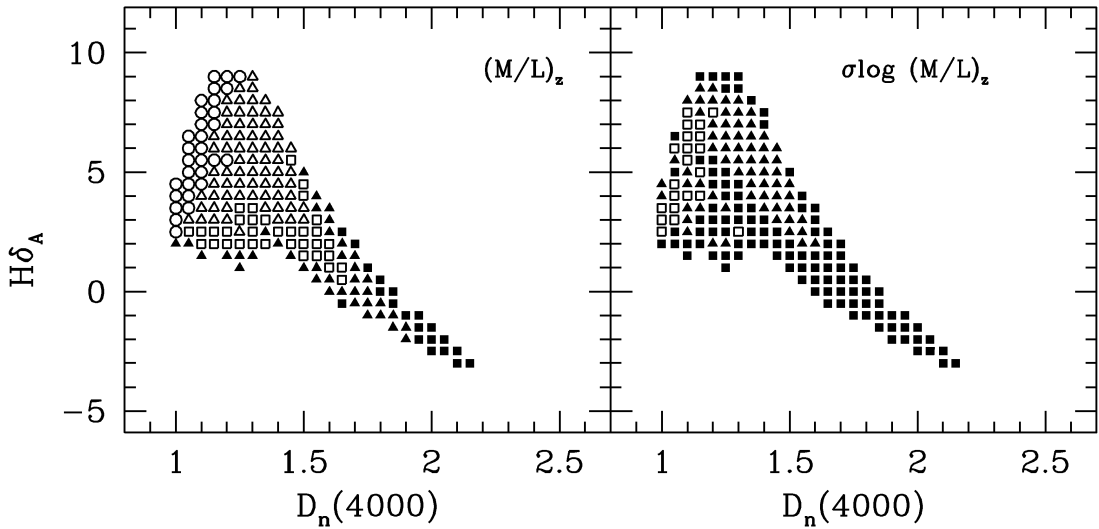


Figure 5. Left: the $D_n(4000)$ – $H\delta_A$ plane has been binned and coded to reflect the average z -band mass-to-light ratios of the simulated stellar populations that fall into that bin. Solid squares indicate regions with $\log (M/L)_z > 0.2$, solid triangles are for $0.05 < \log (M/L)_z < 0.2$, open squares are for $-0.1 < \log (M/L)_z < 0.05$, open triangles for $-0.4 < \log (M/L)_z < -0.1$ and open circles are for $\log (M/L)_z < -0.4$. Right: the plane has been binned and coded to reflect the 1σ dispersion in the z -band mass-to-light ratios. Solid squares indicate regions with $\sigma_{\log (M/L)_z} < 0.1$, solid triangles are for $0.1 < \sigma_{\log (M/L)_z} < 0.15$ and open squares are for $\sigma_{\log (M/L)_z} > 0.15$.

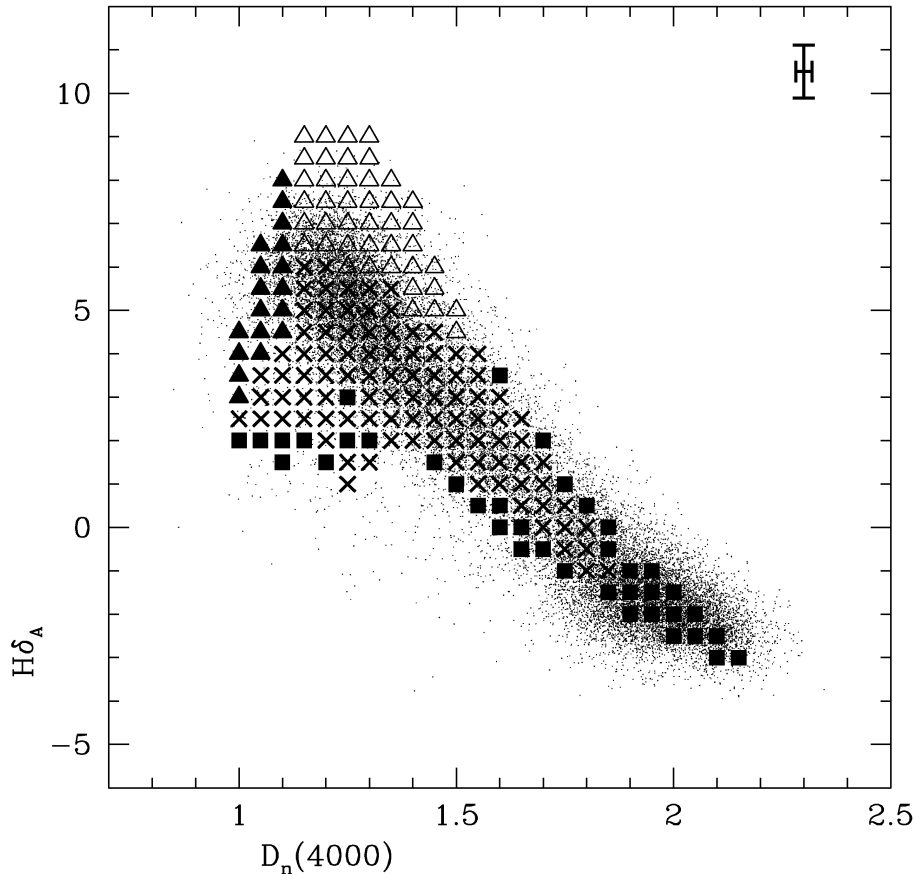


Figure 6. The $D_n(4000)$ – $H\delta_A$ plane has been binned and coded to reflect the fraction of simulated galaxies with F_{burst} in a given range. Open triangles indicate regions where 95 per cent of the model galaxies have $F_{\text{burst}} > 0.05$ and the onset of the burst occurred more than 0.1 Gyr ago. Filled triangles indicate regions where 95 per cent of the model galaxies have $F_{\text{burst}} > 0.05$ and the onset of the burst occurred less than 0.1 Gyr ago. Solid squares indicate regions where 95 per cent of the model galaxies have $F_{\text{burst}} = 0$. Crosses indicate all other regions covered by the model galaxies.

formation histories in the library. This is discussed in more detail in Section 6.2.

For illustrative purposes, we superpose the same subset of SDSS galaxies plotted in Fig. 3 on our colour-coded grid. Once again we see that there is an excellent match between the area of the diagram occupied by the models and the data. There are also a significant number of galaxies that lie within the blue bursty region of the plot. A careful analysis of the observational errors is required before one can assess what fraction of the objects are ‘true’ bursty systems. This is discussed in more detail in Paper II (Kauffmann et al. 2003).

5 PARAMETER ESTIMATION FROM THE DATA

In this section, we apply our method to our sample of SDSS galaxies to estimate parameters such as burst mass fractions, stellar masses and dust attenuations. For each galaxy in the sample, we have a measurement of $D_n(4000)$ and $H\delta_A$ as well as an estimate of the error in these measurements. The likelihood that a galaxy has a given value of a parameter is evaluated by weighting each model in the library by the probability function $\exp(-\chi^2/2)$ and then binning the probabilities as a function of the parameter value (see Appendix A). The most probable value of the parameter can be taken as the peak of this distribution; the most typical value is its median. We

define the 95 per cent confidence interval by excluding the 2.5 per cent tails at each end of the distribution.

5.1 Estimated versus observed values

When the observational uncertainty in a spectroscopic index is large, the best estimate of its true value, taking into account the a priori physical constraints in the population synthesis models, may be significantly different from the observed value. From now on, we will use the median value of the derived probability distributions as our ‘best’ estimate of these parameters (in practice, the peak and the median usually give similar answers). It is informative to compare the *estimated* values of $D_n(4000)$ and $H\delta_A$ with the *observed* values of the same parameters. The results of this comparison are shown in Fig. 7. For $D_n(4000)$, the estimated and observed values are usually equal to well within the 1σ observational uncertainty. However, the differences between estimated and observed values of $H\delta_A$ are often considerably larger. The reason for this is that the models are homogeneously distributed in $D_n(4000)$, but heterogeneously distributed in $H\delta_A$ (see Fig. 4). As a result, models with $H\delta_A$ far away from the observed value often contribute significantly to the probability distribution. This is why the distribution of differences between $H\delta_A$ (estimated) and $H\delta_A$ (observed) shown in Fig. 7 is broad compared with the same distribution derived for the $D_n(4000)$ index.

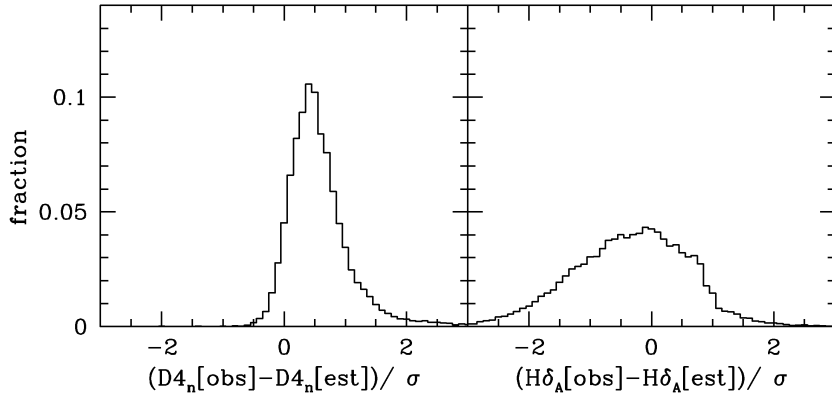


Figure 7. Left: the distribution of the observed value of $D_n(4000)$ minus the estimated one, divided by the 1σ measurement error for all galaxies in the SDSS sample. Right: the same thing except for the $H\delta_A$ index.

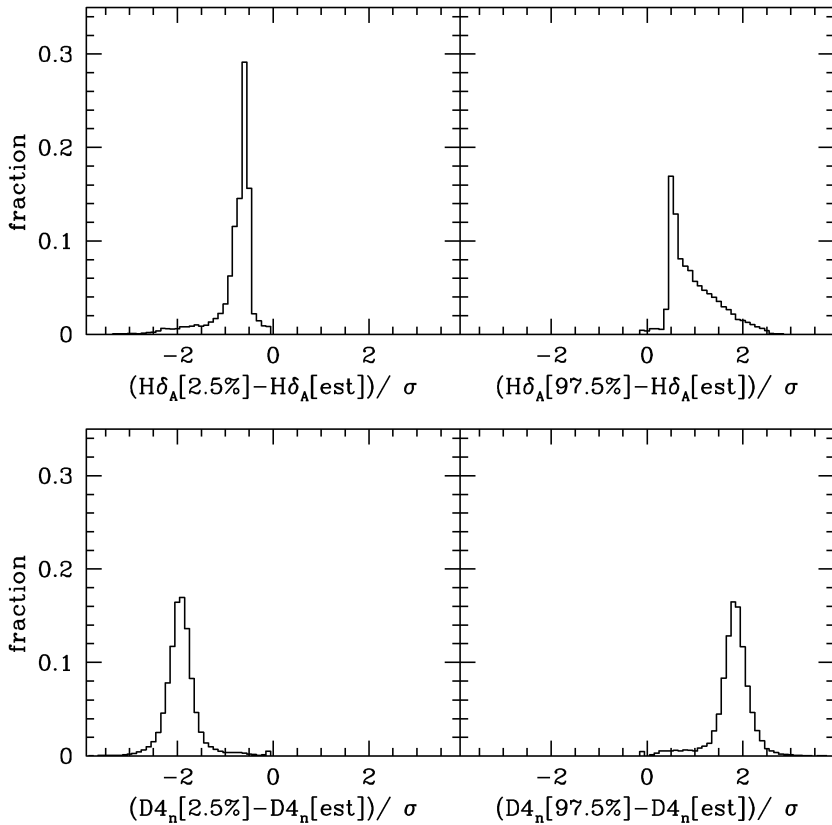


Figure 8. Left: the 2.5 percentile values of the probability distributions of $H\delta_A$ and $D_n(4000)$ minus the best estimates, divided by the 1σ measurement error. Right: the same except for the 97.5 percentile value. These histograms contain the data for our full SDSS sample.

Fig. 8 compares the 2.5 and 97.5 percentile ranges of the estimated values of $D_n(4000)$ and $H\delta_A$ with the observational errorbars. We note that the observational errors on the $D_n(4000)$ index are very small – typically around 0.02 or a few per cent of the total range of values spanned by the models. On the other hand, the $H\delta_A$ index has a typical error of $1\text{--}2\text{ \AA}$, which is more than 10 per cent of the range spanned by the models. As can be seen from Fig. 8, the 2.5 and 97.5 percentile ranges of the probability distribution of $D_n(4000)$ correspond extremely well to the 2σ observational errors. However, the same is not true for $H\delta_A$. Because the error bars on this index are large, the range of acceptable $H\delta_A$ values is strongly constrained by the region of parameter space occupied by the models. As a

result, 2.5 and 97.5 percentile values are typically less than 2σ away from the best estimate. We stress that these effects are caused by genuine *physical constraints*, caused by the fact that $H\delta_A$ can only extend over a limited range of values for all possible star formation histories.

5.2 Estimating burst mass fractions

Fig. 9 shows the probability distributions of the parameter F_{burst} that we derive for three galaxies drawn from our observational sample.

The top galaxy lies in the region of $D_n(4000)\text{--}H\delta_A$ parameter space occupied by galaxies that have formed stars continuously

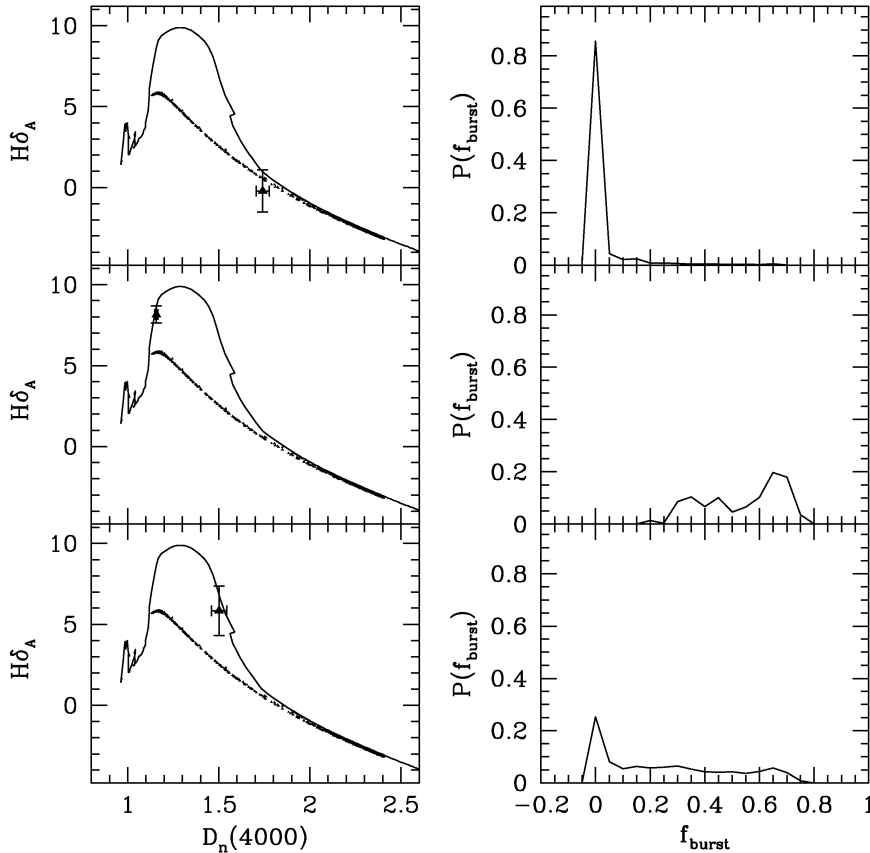


Figure 9. The left-hand panels show the location of three example galaxies in the $D_n(4000)$ – $H\delta_A$ plane. Error bars indicate the measurement errors of the $D_n(4000)$ and $H\delta_A$ indices. The right-hand panels show the probability distributions of the parameter F_{burst} for each galaxy.

over the past few Gyr. This is reflected in the derived probability distribution, which is sharply peaked at a value of $F_{\text{burst}} = 0$. There is a small tail towards non-zero values of F_{burst} , reflecting the fact that the galaxy could have had a small burst of star formation in the past that would not be detectable at the present day.

The middle galaxy lies well away from the locus of continuous star formation models. $D_n(4000)$ and $H\delta_A$ are both measured with high accuracy. As a result, our derived probability distribution indicates that this galaxy *must* have formed more than approximately 25 per cent of its stars in a recent burst. The value of F_{burst} is not very well constrained. This reflects the so-called age/mass degeneracy: a large burst that occurred long ago is indistinguishable from a smaller burst that occurred more recently.

The bottom galaxy lies away from the locus of continuous models, but the error on its $H\delta_A$ index is much larger than that of the middle galaxy. The median value of the probability distribution indicates that a *typical* galaxy with the same $H\delta_A$ and $D_n(4000)$ index measurements will have experienced a burst during the past 2 Gyr. However, one cannot say with any degree of confidence that this particular galaxy must have undergone such a burst.

Our method thus provides us with an objective way of defining a sample of ‘post-starburst’ galaxies from the data. We study the properties of such a sample in detail in Paper II.

5.3 Estimating the attenuation of starlight by dust

So far, we have only calculated mass-to-light ratios and colours of the stellar populations of galaxies. We have not taken into account

the attenuation of the starlight by dust in the interstellar medium (ISM). In the z band, dust attenuation is not expected to be large, but it may nevertheless have a substantial impact on our analysis of mass-to-light ratios, particularly if certain kinds of galaxies are much more dusty than others.

We can use our models to estimate the degree of dust attenuation by comparing our best estimate of the colours of the galaxies from our model library, to the observed colour of the galaxy. Ideally we should use photometry that is matched to the fibre aperture to estimate the dust attenuation. We have chosen to convolve the spectra in our sample with the SDSS g -, r - and i -band filter functions in order to generate a set of synthetic ‘spectral magnitudes’ that can be compared with the models. We have tested the accuracy of our spectrophotometry by comparing the spectral magnitudes of stars drawn from the SDSS to the PSF magnitudes output by the photometric pipeline PHOTO (see Tremonti et al., in preparation, for more details). We have also subtracted off the main emission lines, including $H\alpha$, $[N\text{ II}]$ and $[S\text{ II}]$, to generate a set of true ‘stellar magnitudes’ for our galaxies.

In Fig. 10 we compare the $g - r$ versus $r - i$ colours generated from the spectra (black points) with the colours of the galaxies in our library (blue points). Results are shown for a random subset of our sample of 120 000 galaxies. We plot observer-frame colours at two different redshifts: $z = 0.03$ and 0.11. In the left-hand panels, we show colours without any correction for emission lines. The right-hand panels show what happens when emission lines are removed from the spectra. Over certain redshift ranges, the effect of emission lines on the colours can be large. The $r - i$ colour is strongly affected

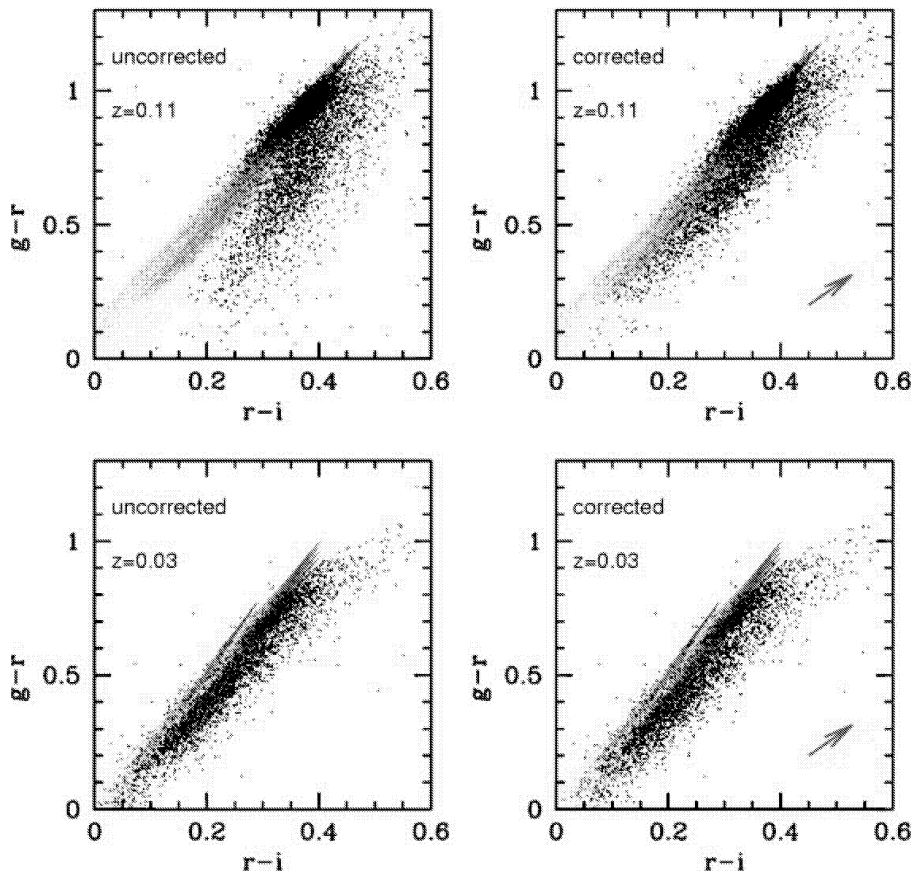


Figure 10. The observed $g-r$ versus $r-i$ spectral colours of a representative subset of SDSS galaxies (black points) are compared with our Bruzual–Charlot model grid (blue points) at $z = 0.03$ and 0.11 . The colours have been computed by convolving the spectra with the SDSS filter functions. In the right-hand panels, the colours are computed after emission lines have been removed from the spectra. The predicted reddening vector assuming an attenuation law of the form $\tau_\lambda \propto \lambda^{-0.7}$ is shown as a red arrow.

by emission at $z \sim 0.1$, because a set of three strong lines ($H\alpha$, $[N\text{ II}]$ and $[S\text{ II}]$) are positioned near the edges of the r and i passbands.

The right-hand panels of Fig. 10 show that the data is still offset from the models, even after we have corrected for emission lines. This offset is caused by dust reddening. The red arrow on the plot indicates the direction of the reddening vector, assuming an attenuation law of the form $\tau_\lambda \propto \lambda^{-0.7}$. The length of the arrow is appropriate for a galaxy with $\tau_V = 0.5$, which is typical for spiral galaxies. We see that reddening will move galaxies systematically to the right of the locus occupied by our models.

We have used the difference between model colours and the measured colours to calculate the reddening for each galaxy in our sample. By extrapolating to the z band using a standard attenuation curve of the form $\tau_\lambda \propto \lambda^{-0.7}$, we obtain an estimate of A_z , the attenuation in the z band expressed in magnitudes. We note that the shape of the attenuation curve determined from direct observations resembles a power law with a slope of ~ -0.7 over a wavelength range from 1250 to 8000 Å (Calzetti, Kinney & Storchi-Bergmann 1994). Models based on a two-component ISM suggest that the extinction curve may be slightly steeper than this at longer wavelengths (Charlot & Fall 2000), but we will use a single power law for simplicity. In practice, we find that comparing $g-r$ or $r-i$ colours yields very similar attenuation values for most galaxies if the colours are corrected for nebular emission.

The distribution of A_z for our full sample of SDSS galaxies is shown in Fig. 11. The errors in our synthesized magnitudes are

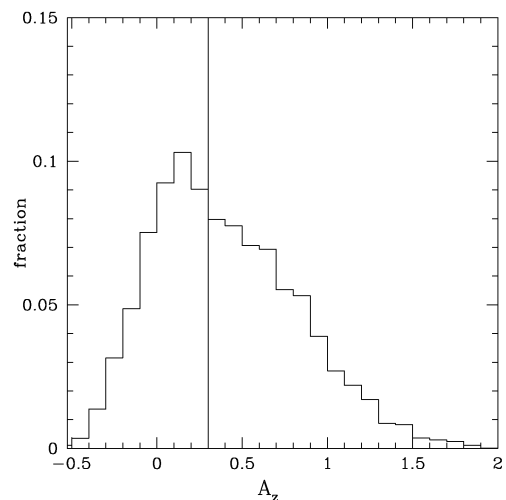


Figure 11. The distribution of the estimated values of the dust attenuation in the z band for all the galaxies in the sample. The median value is shown as a vertical line.

extremely small and the formal 1σ error on our estimate of A_z is typically around ± 0.12 mag. This does not take into account systematic errors that may arise as a result of calibration problems. Fig. 11 shows that the typical attenuation in the z band is quite

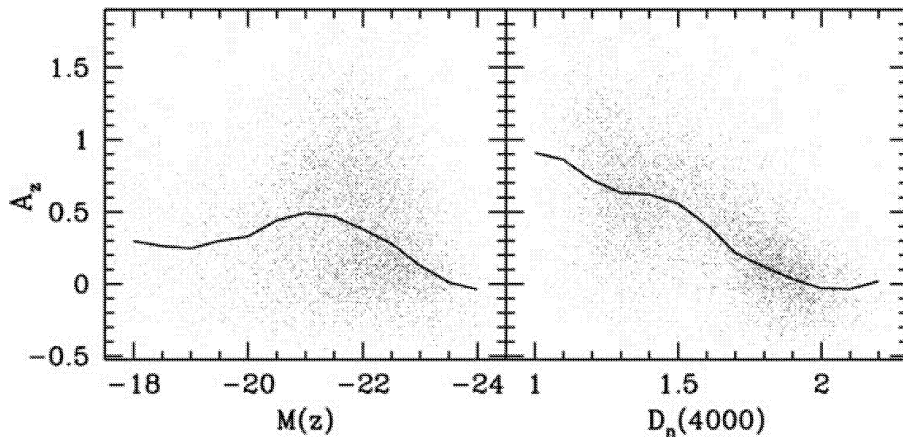


Figure 12. Left: A_z is plotted as a function of z -band absolute magnitude for a random subsample of galaxies. The solid line shows the running median of the distribution for the full sample. Right: A_z is plotted as a function of $D_n(4000)$.

small. The median value of A_z is 0.3 mag. Nevertheless, there is a long tail to high values of A_z . More than 5 per cent of galaxies in the sample are attenuated by more than a magnitude in the z band. The dependences of A_z on absolute magnitude and on $D_n(4000)$ are shown in Fig. 12. At luminosities below L_* , the median attenuation increases for more luminous galaxies. At luminosities above L_* , the median attenuation drops sharply. This can be explained by the fact that the most luminous galaxies are predominantly early-type systems that contain little dust. This is shown more clearly in the right-hand panel of Fig. 12, where we see that galaxies with $D_n(4000) > 1.8$ have $A_z = 0$ on average. Fig. 12 also shows that the galaxies with the youngest stellar populations [small values of $D_n(4000)$] are the most attenuated by dust. This is expected, because galaxies with young stars contain more gas and hence more dust than galaxies with old stellar populations.

5.4 Estimating stellar masses and mass-to-light ratios

In this section, we present estimates of the stellar masses and mass-to-light ratios of the galaxies in our sample. To estimate the stellar mass, we first need to estimate the dust-correction to the observed z -band magnitude of the galaxy. When estimating stellar masses and mass-to-light ratios, we exclude models with $r - i$ colours redder than the observed colour, because this would give negative attenuation corrections, which are unphysical. For each acceptable model, the stellar mass is computed by multiplying the dust-corrected luminosity of the galaxy by the stellar mass-to-light ratio predicted by the model. The best estimate of the mass is then obtained by weighting each model by the probability function in the usual way. Note that in the calculation of our stellar masses, we are extrapolating the mass-to-light ratios and A_z values estimated within the fibre to the galaxy as a whole.

In the top panel of Fig. 13, we plot the z -band stellar mass-to-light ratios estimated from the model as a function of z -band absolute magnitude (corrected to $z = 0.1$) for all the galaxies in our sample. The mass-to-light ratios are plotted in solar units, where we have adopted $M_\odot(z = 0.1) = 4.51$ (Blanton et al. 2002b). As can be seen, the distribution of $(M/L)_z(\text{model})$ is strongly dependent on galaxy luminosity. Almost all very luminous galaxies have high mass-to-light ratios. Faint galaxies span a wider range in $(M/L)_z(\text{model})$. For guidance, we have marked the value of $(M/L)_z(\text{model})$ for a galaxy that has formed stars at a constant rate over a Hubble time as a line on the plot. Galaxies with mass-to-light ratios lower than this value

have had star formation histories that are more weighted towards the present than continuous star formation lasting 10–12 Gyr. Only a few of the most luminous galaxies fall into this category, but at faint magnitudes many galaxies have formed a large fraction of their stars at late times.

The bottom panel of Fig. 13 shows $(M/L)_z(\text{model})$ as a function of the standard concentration parameter C , defined as the ratio $R90/R50$, where $R90$ and $R50$ are the radii enclosing 90 and 50 per cent of the Petrosian r -band luminosity of the galaxy. It has been shown by Shimasaku et al. (2001) and Strateva et al. (2001) that for bright galaxies, there is a good correspondence between the concentration parameter and the ‘by-eye’ classification into Hubble type, but there is some disagreement concerning the value of C that marks the boundary between early- and late-type galaxies. Strateva et al. (2001) claim that galaxies with $C > 2.6$ are mostly early-type systems, whereas spirals and irregulars have $2 < C < 2.6$. Not surprisingly, our stellar mass-to-light ratios are also correlated with concentration parameter, with concentrated (early-type) galaxies exhibiting higher and more uniform values of $(M/L)_z(\text{model})$ than less concentrated (late-type) galaxies.

In Fig. 14, we plot mass-to-light ratios defined in a different way:

$$\frac{M}{L}(\text{galaxy}) = \frac{\text{total mass in stars}}{K\text{-corrected luminosity}}. \quad (2)$$

The total mass in stars is computed by multiplying the dust-corrected and K -corrected z -band luminosity of the galaxy by our estimate of the z -band mass-to-light ratio of its stellar population. $M/L(\text{galaxy})$ thus tells us how a given *observed* luminosity translates into stellar mass. In Fig. 14, we show results in four of the five SDSS bands (g , r , i and z). We do not show results for the u band because of difficulties with the K -corrections. The median value of the mass-to-light ratio in each absolute magnitude bin is shown as a solid symbol. Solid errorbars mark the 25th to 75th percentile ranges of the distributions. Dotted errorbars mark the fifth to 95th percentile ranges. As can be seen, the median mass-to-light ratio first increases with luminosity and then appears to flatten. The scatter in $M/L(\text{galaxy})$ at fixed luminosity decreases at longer wavelengths: it is more than a factor of 2 larger in the g band than in the z band.

In order to make a comparison with related work, we have plotted as a thick solid line the mean relation between $(M/L)_r(\text{dynamical})$ and r -band magnitude derived by Bernardi et al. (2002) for a sample of early-type galaxies drawn from the SDSS. In this analysis

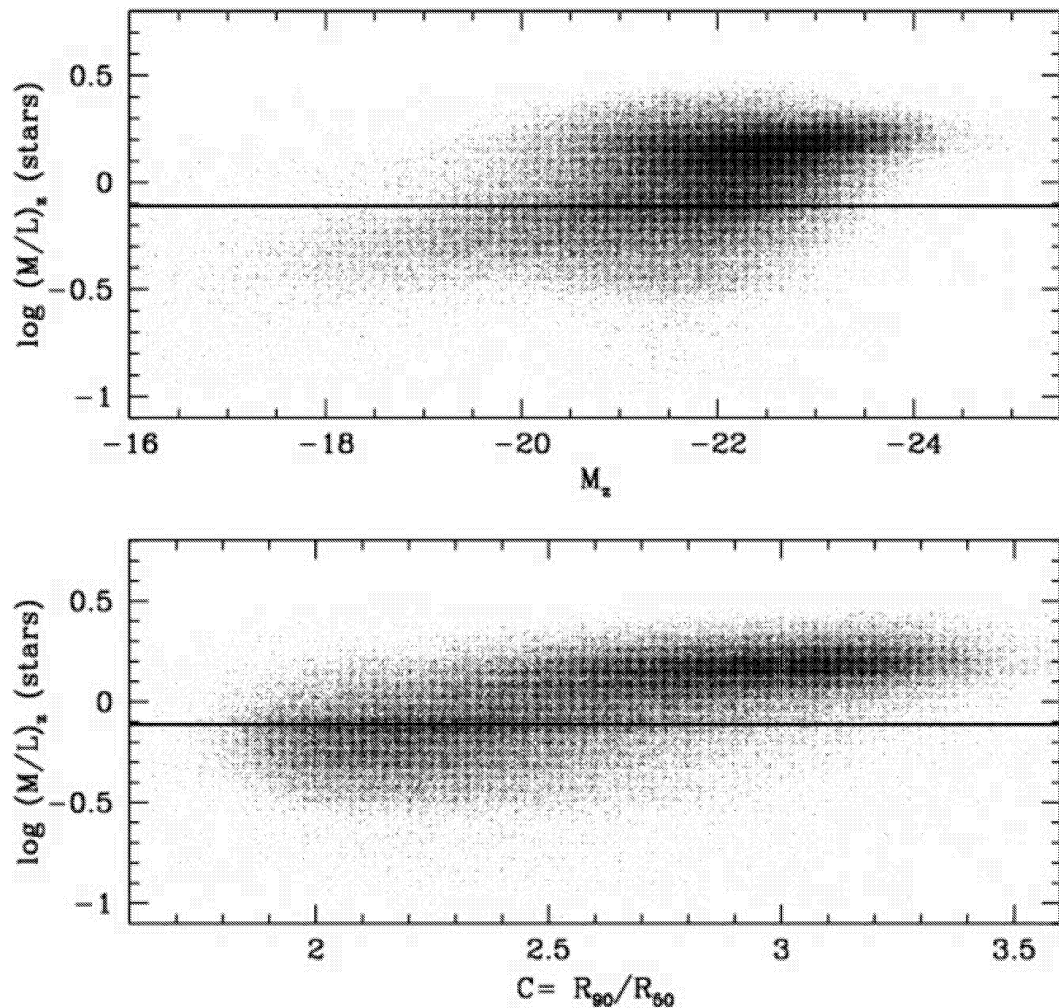


Figure 13. Top: our estimate of z -band mass-to-light ratios of the stellar populations of the galaxies in our sample is plotted as a function of K -corrected z -band absolute magnitude for all galaxies in the sample. Bottom: the mass-to-light ratio is plotted as a function of r -band concentration parameter for all galaxies in the sample. The line indicates the value of $(M/L)_z(\text{stars})$ for an unextinct galaxy that has been forming stars at a constant rate for a Hubble time.

$M/L \propto R_0 \sigma^2 / L$, where R_0 is the effective radius of the galaxy and σ is the line-of-sight velocity dispersion of the stars measured in a 3-arcsec aperture. It is interesting that the relation derived by Bernardi et al. agrees well with our $M/L(\text{galaxy})$ estimates for less luminous galaxies, but lies above our estimates for brighter galaxies. This may be an indication that more luminous galaxies contain more dark matter than less luminous galaxies. We caution, however, that a more careful analysis is required because the Bernardi et al. sample is carefully selected to contain only galaxies with pure early-type spectra, whereas our sample includes all galaxies. Note that if we had assumed a Salpeter rather than a Kroupa (2001) IMF, our stellar mass estimates would have been around a factor of 2 larger. For lower-mass ellipticals, there would then be a clear contradiction with the dynamically derived mass estimates.

The distribution of formal errors on our stellar mass estimates is shown in Fig. 15. We plot the distribution of the 95 per cent confidence range in $\log M_*$, i.e. the range of values of $\log M_*$ obtained when the 2.5 per cent tails at each end of the probability distribution of $\log M_*$ are excluded. For a Gaussian distribution of errors, this corresponds to four times the standard error in the mass estimate. As can be seen, the 95 per cent confidence interval is typically around a factor of ~ 2 in mass. The errors are smaller for older galaxies with

larger 4000-Å breaks than for younger galaxies with smaller break strengths.

6 SOURCES OF SYSTEMATIC ERROR

Fig. 14 indicates that the formal errors on our stellar mass estimates are small. There are, however, quite a few sources of possible systematic error. In this section, we explore some of these in more detail.

6.1 Aperture effects

The $D_n(4000)$ and $H\delta_A$ indices measured from the SDSS spectra reflect the properties of the starlight that found its way down a 3-arcsec diameter fibre that has been positioned as close as possible to the centre of the galaxy. One may thus wonder to what extent our estimates of $(M/L)_z$ may be biased because the index measurements are not accurately reflecting the stellar content of the whole galaxy. In particular, aperture bias could well be a serious problem for spiral galaxies, where the index measurements may be appropriate for the central bulge component, but not for the outer disc where most of the star formation is taking place.

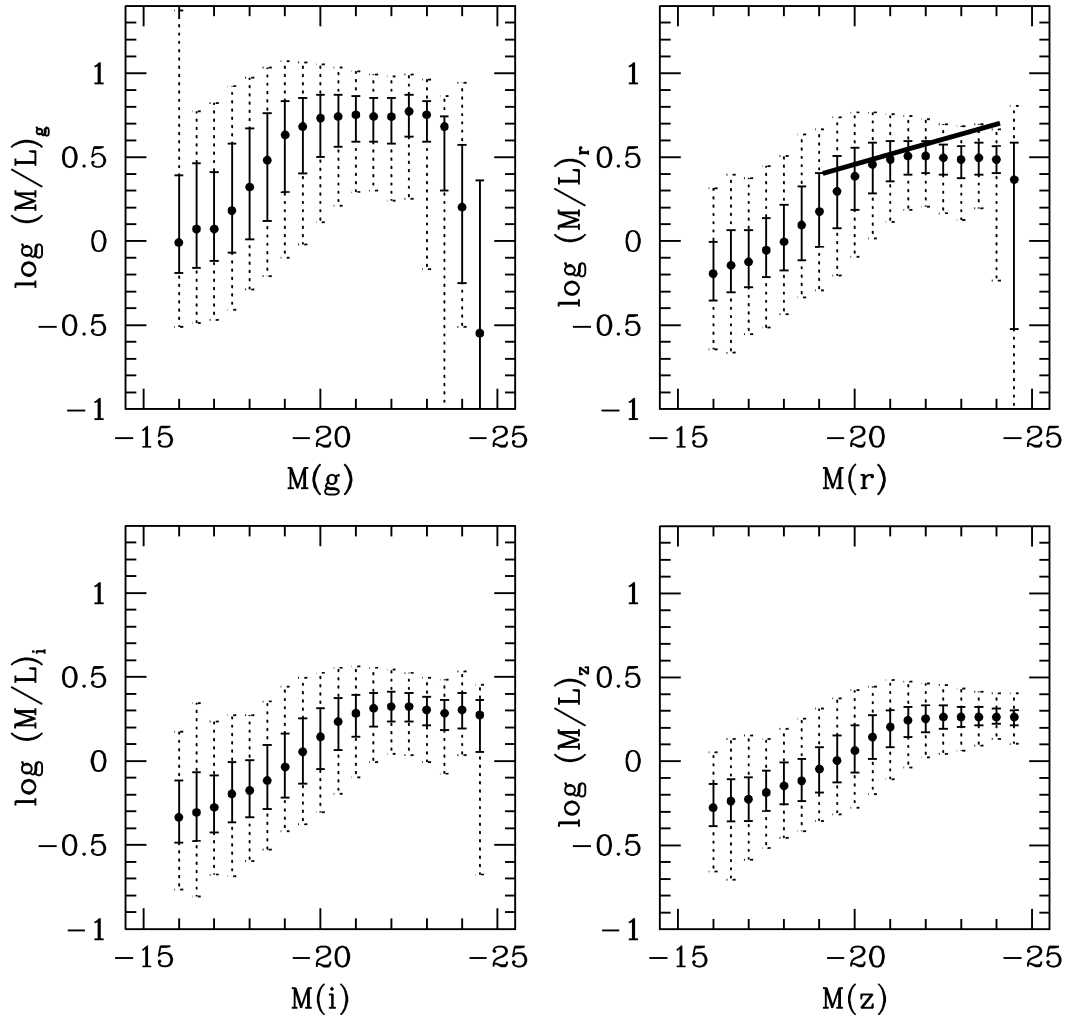


Figure 14. The total stellar mass of a galaxy divided by its observed luminosity (K -corrected to $z = 0.1$) is plotted as a function of absolute magnitude in four SDSS bands. The solid symbols indicate the median mass-to-light ratio at a given magnitude, the solid errorbars indicate the 25th to 75th percentile ranges of the distribution and the dotted errorbars indicate the fifth-95th percentile ranges. Mass-to-light ratios are plotted in solar units where $M_{\odot g} = 5.45$, $M_{\odot r} = 4.76$, $M_{\odot i} = 4.58$ and $M_{\odot z} = 4.51$ at $z = 0.1$ (Blanton et al. 2002b). The thick solid line is the mean relation between dynamical M/L (estimated from the stellar velocity dispersion) and r -band magnitude for a sample of early-type galaxies from Bernardi et al. (2002).

It is possible to address the effect of aperture bias in a statistical way by comparing the observed stellar indices and the derived M/L values for similar galaxies viewed at different distances from us. If aperture bias is important, one should see a trend in these quantities with distance.

This is illustrated in Figs 16 and 17. We plot the index $D_n(4000)$ and the z -band mass-to-light ratio $(M/L)_z$ as a function of ‘normalized’ distance z/z_{\max} , where z_{\max} is the redshift at which the galaxy drops out of the survey. Normalizing by z_{\max} takes care of any selection effects that arise when one divides up the sample in different ways. Note that as expected, galaxies in the survey are distributed uniformly in the quantity V/V_{\max} , so there are many more objects in the bins with z/z_{\max} values close to 1.

Fig. 16 shows the variation in the 4000-Å break as a function of normalized distance. We see that both the size and the sense of the effect depend strongly on the absolute magnitude of the galaxy. Galaxies with luminosities $\sim L_*$ [$M_*(z) = -22.3$] exhibit the strongest trend with z/z_{\max} . More distant galaxies have younger stellar populations than nearby objects, as expected if the spectra are preferentially sampling the bulges of nearby galaxies.

Fig. 17 shows how the dust attenuation in the z band varies as a function of distance. Our results indicate that A_z increases towards the centres of low-luminosity galaxies, but in galaxies with luminosities $\sim L_*$, the attenuation increases towards the outer regions. In the most luminous galaxies in our sample, the attenuation does not appear to vary strongly as a function of radius. The simplest interpretation of these trends is that our low-luminosity sample is dominated by disc galaxies, which are known to have significant metallicity gradients (e.g. Zaritsky, Kennicutt & Huchra 1994). If dust content correlates with metallicity, one might expect the light from stars in the inner parts of these galaxies to be more attenuated. Galaxies with luminosities $\sim L_*$ are composite systems consisting of both a bulge and a disc; starlight from the bulge is expected to be less attenuated than that from the disc. The highest luminosity galaxies are primarily ellipticals, which contain very little dust and have no appreciable gradients in A_z .

Finally, Fig. 18 shows the trend in our estimates of $(M/L)_z$ with distance. As can be seen, the effect of aperture on the mass-to-light ratio is relatively small. For L_* galaxies, our estimate of the median $(M/L)_z$ decreases by 0.12 dex from one edge of the survey to the

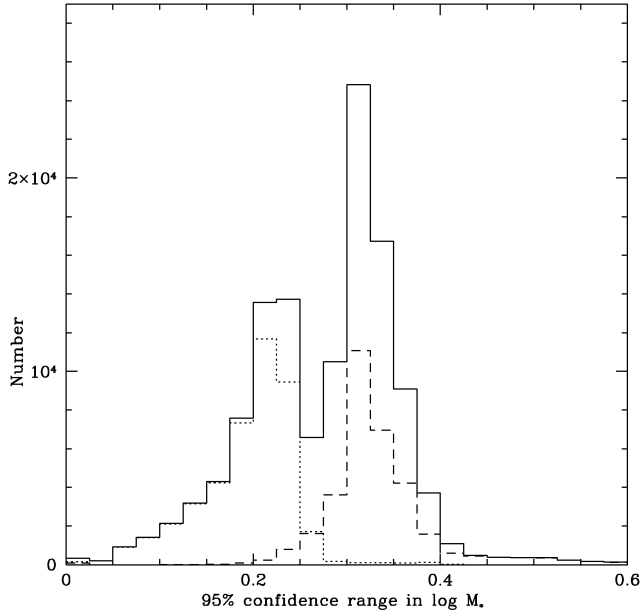


Figure 15. The distribution of errors in our stellar mass estimates. The quantity plotted is the full length of the 95 per cent confidence interval in $\log M_*$. The solid histogram shows the distributions for all galaxies in the sample. The dotted histogram is for the subset of galaxies with $D_n(4000) > 1.8$ and the dashed histogram is for galaxies with $D_n(4000) < 1.4$.

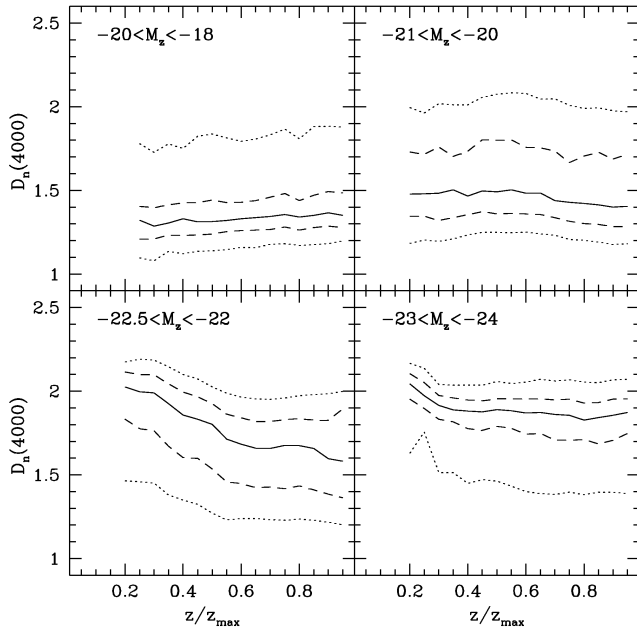


Figure 16. The $D_n(4000)$ index is plotted as a function of z/z_{\max} for galaxies in different ranges of z -band absolute magnitude. The solid line indicates the median of the distribution as a function of z/z_{\max} . The dashed lines indicate the 25th and 75th percentiles. The dotted lines indicate the fifth and 95th percentiles.

other. For brighter and fainter galaxies, the effect is even smaller. Unfortunately, it is not possible to use the relations shown in Figs 16–18 to estimate the true global mass-to-light ratio of a given type of galaxy. Even at the outer limit of the survey, the median fraction of the total galaxy light that enters the fibre is around 50 per cent. A sample of galaxies with large-aperture spectra is required for this

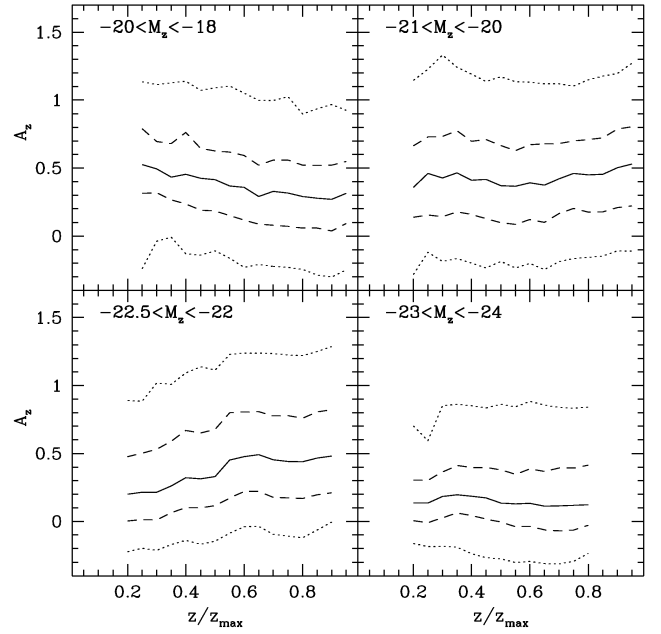


Figure 17. The dust attenuation in the z band A_z is plotted as a function of z/z_{\max} for galaxies in different ranges of z -band absolute magnitude.

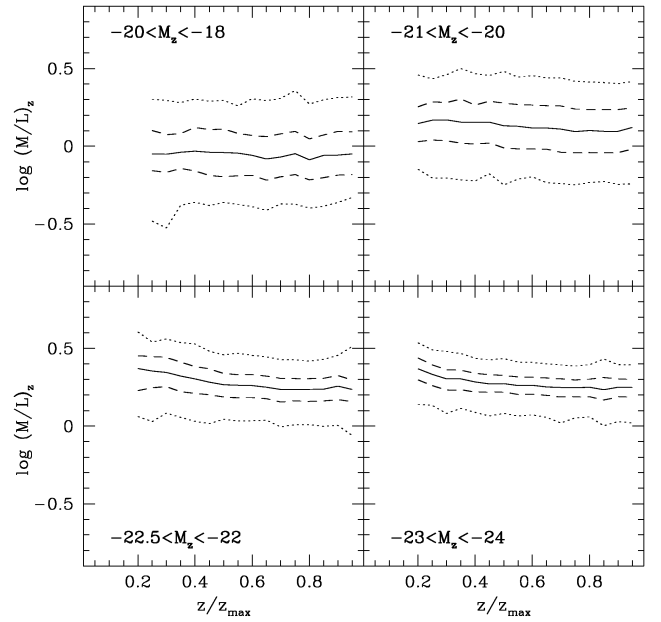


Figure 18. The stellar mass-to-light ratio in the z band is plotted as a function of z/z_{\max} for galaxies in different ranges of z -band absolute magnitude.

purpose. Nevertheless, our plots make it clear that the variations in M/L as a function of luminosity and concentration are substantially larger than any biases induced by aperture effects.

6.2 The choice of prior

It is important to understand how our choice of priors may bias our estimates of parameters such as mass-to-light ratios or burst mass fractions. The assumed prior will have little influence if error bars are small and the problem is well constrained. Because the errors on the $H\delta_A$ index are of the same order as the total spread of values in the

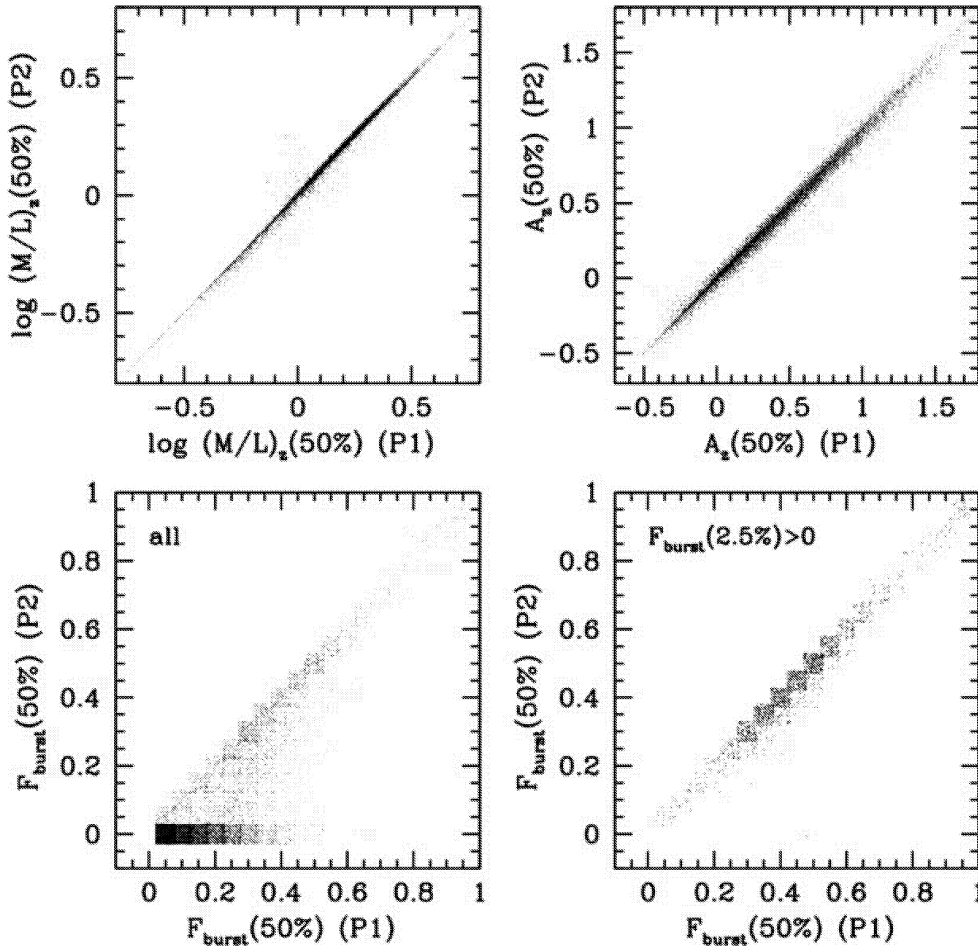


Figure 19. The derived values of the mass-to-light ratio $(M/L)_z$, the attenuation A_z , the median of the likelihood distribution of F_{burst} , and the lower 2.5 percentile value of this distribution are compared for two different choices of prior.

model grid, parameters such as F_{burst} , which depend strongly on the value of the $H\delta_A$ index, will be influenced by the mix of star formation histories contained in our model library.

This is illustrated in Fig. 19 where we compare, for two different choices of prior, our best estimates of mass-to-light ratio $(M/L)_z$, attenuation A_z and burst mass fraction F_{burst} . P1 is our ‘standard’ prior, described in detail in Section 4. P2 is a modified prior where we have reduced by a factor of 10 the probability of all models with bursts in the latter 2 Gyr. In the first three panels, we plot the median of the likelihood distribution obtained using P2 versus the median obtained using P1. In the F_{burst} panel, we only plot those galaxies that have $F_{\text{burst}}(50 \text{ per cent}) > 0$ for either P1 or P2. As can be seen, our estimates of $(M/L)_z$ and A_z are insensitive to the choice of prior. On the other hand, $F_{\text{burst}}(\text{median})$ does depend strongly on the fraction of galaxies in the model grid that have experienced recent starbursts.

In the fourth panel, we compare the median of the likelihood distributions of F_{burst} for the *subset* of galaxies with $F_{\text{burst}}(2.5 \text{ per cent}) > 0$ for either prior, i.e. we restrict the sample to galaxies that are very strongly constrained to have experienced a recent starburst. The lower right-hand panel of Fig. 19 demonstrates that for these galaxies, $F_{\text{burst}}(50 \text{ per cent})$ is insensitive to the choice of prior.

This demonstrates that it is valid to use the criterion $F_{\text{burst}}(2.5 \text{ per cent}) > 0$ to select subsamples of starburst and post-

starburst galaxies from our full data set. $F_{\text{burst}}(50 \text{ per cent})$ then provides the best estimate of the fraction of the total mass in stars formed in the burst mode over the past 2 Gyr.

6.3 Other sources of systematic error

(i) *Stellar population models.* Fig. 2 indicates that the differences in the predicted values of $D_n(4000)$ and $H\delta_A$ at a given stellar age for three different input stellar libraries are comparable to the measurement errors for those indices. Unfortunately, we are only able to carry out this test at solar metallicity, so we are unable to carry out a fully rigorous analysis of the systematic uncertainty arising from our calibration of these indices.

(ii) *IMF.* All of our derived parameters are tied to a specific choice of IMF. Changing the IMF would scale the stellar mass estimates by a fixed factor. For example, changing from a Kroupa (2001) to a Salpeter IMF with a cut-off at $0.1 M_\odot$ would result in a factor of 2 increase in the stellar mass.

(iii) *Calibration errors.* Our dust corrections rely on accurately calibrated spectral magnitudes. Any systematic offsets in the spectrophotometric calibrations will result in systematic errors in these corrections. A full assessment of the accuracy of the wavelength and flux calibration of SDSS spectra will be given in Tremonti et al. (in preparation).

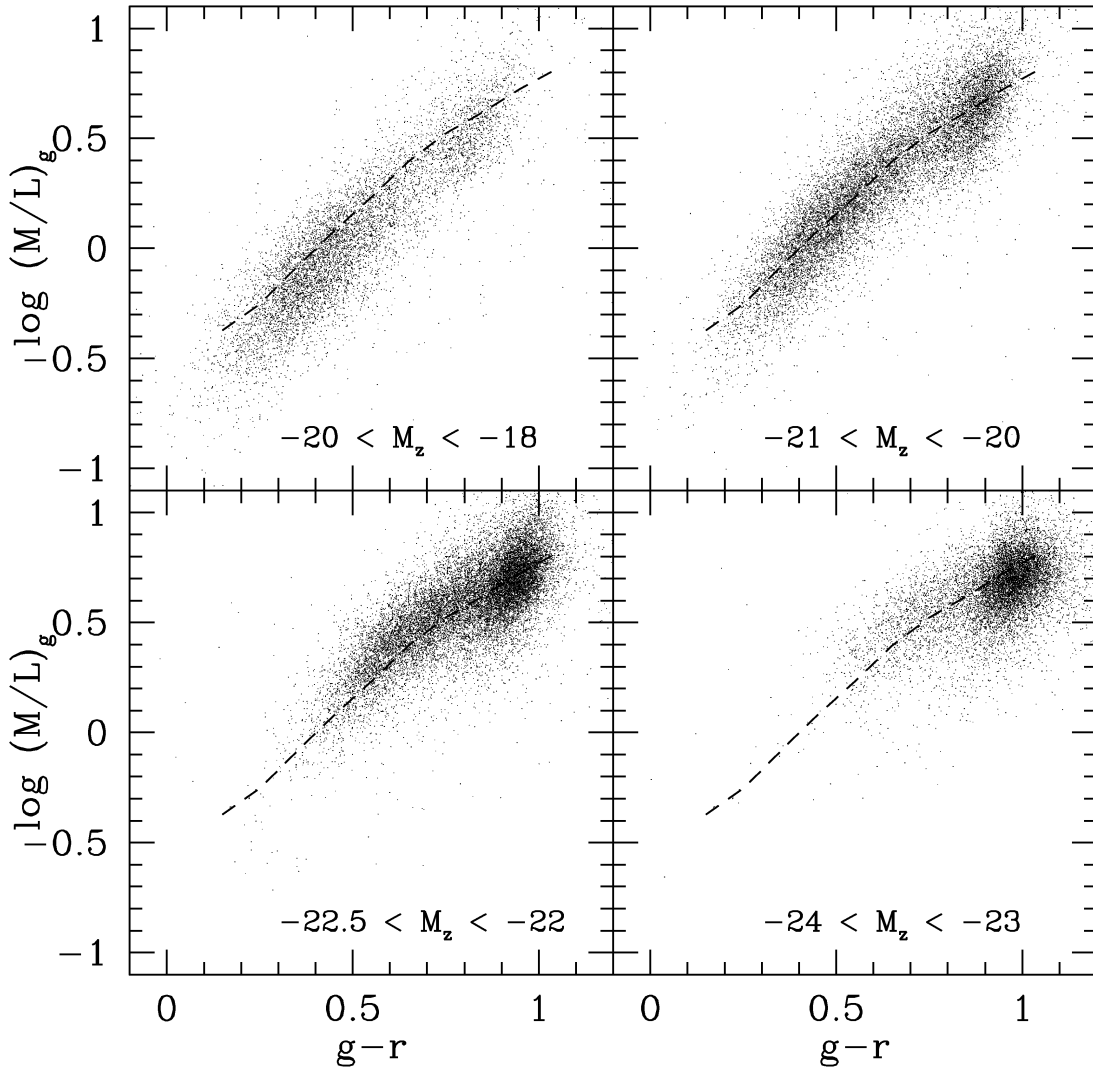


Figure 20. The g -band mass-to-light ratio is plotted as a function of the $g-r$ colour (K -corrected to $z = 0.1$) for galaxies in four different bins of z -band absolute magnitude. The dashed line shows the mean relation evaluated for galaxies with $-21 < M(z) < -20$.

7 COMPARISON WITH COLOUR-BASED METHODS

Most previous attempts to convert from absolute magnitude to stellar mass have used colours to constrain the star formation histories of galaxies (e.g. Bell & De Jong 2001; Brinchmann & Ellis 2000; Cole et al. 2001). Bell & De Jong (2001) argue that there should be a tight relation between the optical colours of spiral galaxies and their stellar mass-to-light ratios. This relation ought to be insensitive to the effects of dust-reddening. Although dust causes colours to become redder, it also makes the galaxy fainter and for a standard dust attenuation curve, the two effects compensate. Bell & De Jong (2001) show that recent bursts of star formation introduce scatter into this relation, but claim that this should not be important for most spirals in Tully–Fisher samples.

It is interesting to see whether the stellar masses derived using our method correlate with the observed optical colours of galaxies. In Fig. 20 we plot the stellar mass-to-light ratio in the g band as a function of the Petrosian $g-r$ colours (K -corrected to $z = 0.1$) for galaxies in four different absolute magnitude ranges. We find that there is a tight relation between colour and the stellar mass-

to-light ratio. The scatter in $\log(M/L)_g$ at given $g-r$ colour is roughly constant at all magnitudes and has an rms value of ~ 0.3 dex. However, the zero-point of the relation shifts systematically by approximately 0.2 dex from the faintest to the brightest galaxies in our sample. At least part of this effect may be caused by the fact that brighter galaxies have stronger colour gradients (Fig. 16) and our mass-to-light ratio will consequently be biased to higher values than those measured from integrated colours. Overall, the agreement is very encouraging, as it suggests that SDSS colours may be used to derive a reasonably accurate estimate of the stellar masses of nearby galaxies when spectroscopic information is missing. Note that the $r-i$ colour would *not* work well because of its sensitivity to emission lines at redshifts $z \sim 0.1$.

8 AN INVENTORY OF THE STELLAR MASS IN THE UNIVERSE

In this section, we compute how galaxies of different types contribute to the total stellar mass budget of the local Universe. Galaxies of different luminosities can be seen to different distances before

dropping out because of the selection limits of the survey. The volume V_{\max} within which a galaxy can be seen and will be included in the sample goes as the distance limit cubed, which results in galaxy samples being dominated by intrinsically bright galaxies. In this paper we use the simplest available method for correcting for selection effects, the V_{\max} correction method (Schmidt 1968). Each galaxy is given a weight equal to the inverse of its maximum visibility volume determined from the apparent magnitude limit of the survey. In order to obtain an estimate of the true number density of galaxies in the Universe, it is necessary to account for galaxies that are missed owing to fibre collisions or spectroscopic failures. This affects around 10–15 per cent of the galaxies brighter than the spectroscopic limit of the survey (Blanton et al. 2001). Here, we focus on the *relative* contribution of different kinds of galaxies to the total stellar mass, so weighting by $1/V_{\max}$ ought to be sufficient. As a check, we have computed the z -band luminosity function for the galaxies in our sample and find that the Schechter function fit given in Blanton et al. (2001) provides an excellent match to the shape of the function we derive.

A compendium of results is presented in Fig. 21. We plot the fraction of the total stellar mass contained in galaxies as a function of their stellar mass, $D_n(4000)$, $g - r$ colour, F_{burst} , size, concentration index and surface mass density. Note that we have adopted a cosmology with $\Omega = 0.3$, $\Lambda = 0.7$ and $H_0 = 70 \text{ km s}^{-1} \text{ Mpc}^{-1}$ in our

calculations. From these plots it is possible to read off the characteristic properties of the galaxies that contain the bulk of the stellar mass in the Universe at the present day. Note that because we have 122 808 galaxies in the total sample, we are able to derive extremely accurate functional forms for these distributions. The bins around the peaks of the distributions shown in Fig. 21 each contain 5000 or more galaxies. Even in the wings, most bins are still sampled by a few hundred objects. In Table 1, we list the median, 1, 5, 25, 75, 95 and 99 per cent percentile values for each of the distributions shown in Fig. 21 (with the exception of F_{burst}).

Our main conclusions are as follows.

(i) The characteristic mass M_{char} of galaxies at the present day, defined as the peak of the distribution function shown in the top left-hand panel of Fig. 21, is $6 \times 10^{10} M_{\odot}$. This agrees reasonably well with the results of Cole et al. (2001). These authors transform the near-infrared luminosity function derived from 2dF/2MASS data to a stellar mass function using a colour-based technique. Their Schechter-function parametrization yields $M_{\text{char}} = 5.6 \times 10^{10} M_{\odot}$ for $H_0 = 70 \text{ km s}^{-1} \text{ Mpc}^{-1}$ and a Kennicutt (1983) IMF, which is fairly close to the Kroupa (2001) IMF that we have assumed.

We find that only 20 per cent of the total stellar mass is contained in galaxies less massive than $10^{10} M_{\odot}$. An even smaller fraction (~ 13 per cent) of the total mass is contained in galaxies less massive

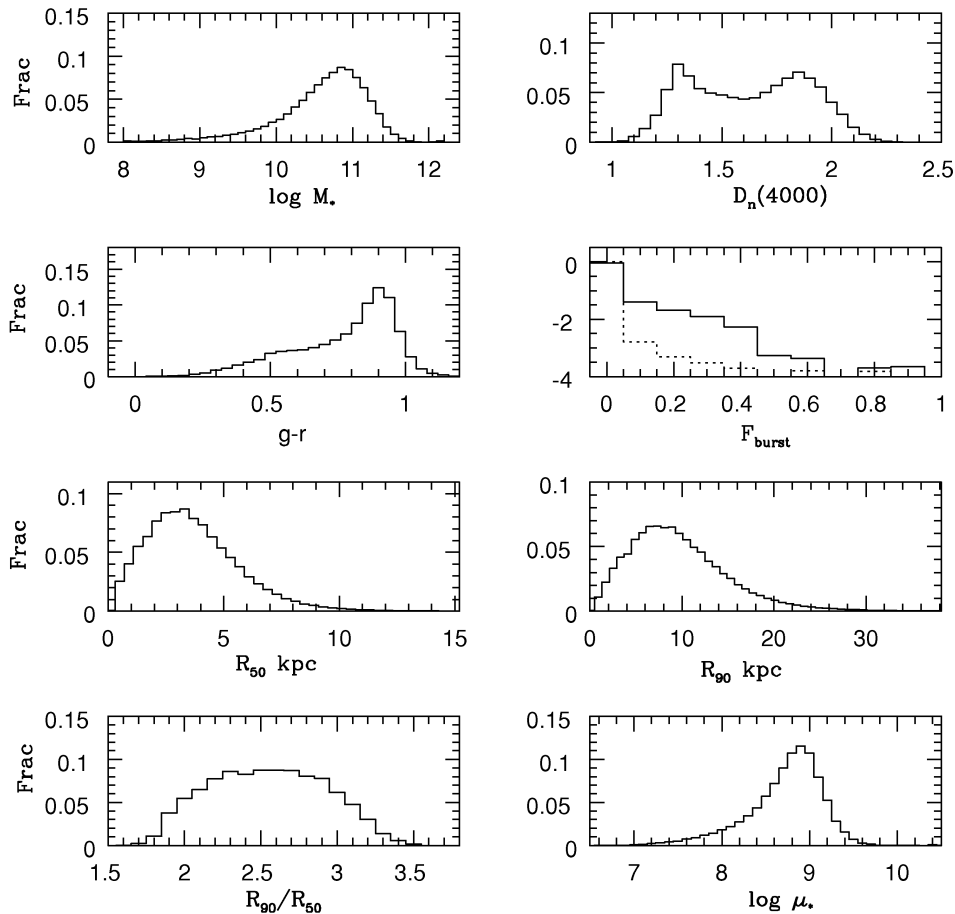


Figure 21. The fraction of the total stellar mass in the Universe contained in galaxies as a function of (i) log stellar mass, (ii) $D_n(4000)$, (iii) $g - r$ colour (K -corrected to $z = 0.1$), (iv) F_{burst} (median) solid and F_{burst} (2.5 per cent) dotted, (v) Petrosian half-light radius in the r band, (vi) Petrosian 90 per cent radius on the r band, (vii) concentration index (R_{90}/R_{50}), (viii) log surface mass density. The fraction is shown linearly in all plots except that for F_{burst} where the logarithm is given.

Table 1. Percentiles of the distribution of the fraction of the total stellar mass contained in galaxies of different types shown in Fig. 21.

Parameter	Median	1 per cent	5 per cent	25 per cent	75 per cent	95 per cent	99 per cent
$\log M_*$ (M_\odot)	10.661	8.573	9.334	10.264	10.958	11.308	11.534
$D_n(4000)$	1.609	1.105	1.120	1.350	1.838	2.012	2.119
$g - r$ ($z = 0.1$)	0.816	0.238	0.380	0.634	0.906	1.095	1.411
R_{50} (kpc)	3.225	0.249	0.740	2.042	4.636	7.190	9.652
R_{90} (kpc)	8.748	0.784	2.075	5.417	12.177	19.386	27.014
$C = R_{90}/R_{50}$	2.493	1.767	1.896	2.201	2.787	3.106	3.284
$\log \mu_*$ ($M_\odot \text{ kpc}^{-2}$)	8.745	7.327	7.810	8.453	8.958	9.242	9.484

than $10^9 M_\odot$. The total stellar mass budget of the Universe is thus heavily weighted towards galaxies that are within a factor of 10 in mass of the Milky Way.

(ii) The $D_n(4000)$ distribution of the stellar mass is strongly bimodal. The first peak is centred at $D_n(4000) \sim 1.3$. Galaxies with break strengths of this value have r -band weighted mean stellar ages of ~ 1 – 3 Gyr and mass-weighted mean ages a factor of ~ 2 larger. Almost all of these galaxies also have emission lines and are thus forming stars at the present day. The second peak is centred at $D_n(4000) \sim 1.85$, a value typical of old elliptical galaxies with mean stellar ages ~ 10 Gyr.

(iii) The $g - r$ colour distribution exhibits a strong red peak, but the blue peak is much less pronounced. This is probably because colours depend both on stellar age and on dust attenuation, whereas $D_n(4000)$ is not affected by dust. Note that Strateva et al. (2001) have also discussed the bimodality in the colour distributions of SDSS galaxies.

(iv) The vast majority (>90 per cent) of the stellar mass is in galaxies that have not formed more than 5 per cent of the stars in a burst over the past 2 Gyr.

(v) The distribution of stellar mass as a function of galaxy half-light radius in the r band (R_{50}) is peaked at ~ 3 kpc. For the radius containing 90 per cent of the light (R_{90}) it is peaked at ~ 8 kpc. More than 90 per cent of the total stellar mass in the Universe resides in galaxies with R_{50} and R_{90} that are within a factor of 3 of these values.

(vi) The distribution of stellar mass as a function of concentration index is broad, with no pronounced peak at any particular value. If we adopt $C = 2.6$ as the demarcation between early- and late-type galaxies, then 50 per cent of the total stellar mass is contained in the early types. If we adopt $C = 3$, then only 10 per cent of the mass is contained in such systems.

(vii) We define the surface mass density μ_* as $0.5M_*/(\pi z_{50}^2)$, where z_{50} is the Petrosian half-light radius in the z band. Most of the stellar mass in the Universe resides in galaxies with μ_* within a factor of 2 of $10^9 M_\odot \text{ kpc}^{-2}$.

9 SUMMARY AND DISCUSSION

We have developed a new method to constrain the past star formation histories of galaxies. It is based on two stellar absorption-line indices, the 4000-Å break strength $D_n(4000)$ and the Balmer absorption-line index $H\delta_A$. Together these two indices allow us to place constraints on the mean age of the stellar population of a galaxy and the fraction of its stellar mass formed in recent bursts.

We have generated a library of Monte Carlo realizations of different star formation histories, which includes bursting and continuous models and a wide range of metallicities. We use the library to generate estimates and confidence intervals for a variety of parameters

for a sample of 122 808 galaxies drawn from the Sloan Digital Sky Survey. These include:

- (i) F_{burst} the fraction of the stellar mass of the galaxy formed in bursts in the past 2 Gyr;
- (ii) A_z the attenuation of the rest-frame z -band light as a result of dust;
- (iii) stellar mass-to-light ratios in the g , r , i and z bands;
- (iv) stellar masses.

Note that the analysis can be extended to include other parameters describing the star formation history of a galaxy, but not all parameters are equally well constrained. For example, the luminosity-weighted or mass-weighted mean stellar ages have large errors, because of the rather strong dependence of the 4000-Å break on metallicity at ages of more than 1–2 Gyr (see Fig. 2).

In the first part of the paper, we have illustrated in detail how our methods can be applied to galaxies in the SDSS and we have estimated the confidence with which we can constrain basic parameters such as stellar mass. In the second part of the paper, we have presented a number of astrophysically interesting applications of our methods.

We have shown that the attenuation of the z -band light as a result of dust depends strongly on both the absolute magnitude and the mean stellar age of a galaxy. We have also studied the distribution of stellar mass-to-light ratios of galaxies as a function of absolute magnitude in the four SDSS passbands. We have shown that the distribution of M/L is strongly dependent on galaxy luminosity in all photometric bands. Almost all very luminous galaxies have high mass-to-light ratios. Faint galaxies have lower mass-to-light ratios, but also span a wider range in M/L . We have also shown that the scatter in M/L at a given luminosity is a factor of ~ 2 smaller in the z band than it is in the g band. Finally, we have computed how galaxies of different types contribute to the total stellar mass budget of the Universe.

In the standard paradigm for structure formation in the Universe, galaxy formation occurs hierarchically through the merging of small protogalactic condensations to form more and more massive systems. In this picture, the contribution of different kinds of galaxies to the stellar mass budget is expected to evolve strongly with redshift. The rate and form of this evolution depend not only on the values of cosmological parameters such as Ω and Λ , but also on the physical processes that control the rate at which stars form in galaxies. For example, if star formation rates are enhanced during galaxy–galaxy mergers, the fraction of stars formed in recent bursts should rise strongly with redshift, simply because merging rates and gas fractions were higher in the past (see, for example, Kauffmann & Haehnelt 2000).

Although it is now clear that the integrated star formation rate density increases strongly to higher redshifts (Madau et al. 1996), it

is still not understood which galaxies undergo the strongest evolution or which physical processes cause galaxies to form stars more rapidly in the past. In the next few years, there will be a number of new large redshift surveys of the faint galaxy population. These surveys will contain enough galaxies to carry out an inventory of the stellar mass at $z \sim 1$. When these results are compared with the distributions derived from the SDSS, it will be possible to draw quantitative conclusions concerning how galaxies have evolved over the past two-thirds of a Hubble time and to begin disentangling the effects of the different processes that may have influenced this evolution.

We thank the anonymous referee for detailed comments that helped improve our methodology.

ACKNOWLEDGMENTS

SC thanks the Alexander von Humboldt Foundation, the Federal Ministry of Education and Research, and the Programme for Investment in the Future (ZIP) of the German Government for their support. The Sloan Digital Sky Survey (SDSS) is a joint project of The University of Chicago, Fermilab, the Institute for Advanced Study, the Japan Participation Group, The Johns Hopkins University, Los Alamos National Laboratory, the Max-Planck Institute for Astronomy (MPIA), the Max-Planck Institute for Astrophysics (MPA), New Mexico State University, Princeton University, the United States Naval Observatory, and the University of Washington. Apache Point Observatory, site of the SDSS telescopes, is operated by the Astrophysical Research Consortium (ARC). Funding for the project has been provided by the Alfred P. Sloan Foundation, the SDSS member institutions, the National Aeronautics and Space Administration, the National Science Foundation, the US Department of Energy, the Japanese Monbukagakusho, and the Max Planck Society. The SDSS Web site is <http://www.sdss.org/>.

REFERENCES

- Balogh M.L., Morris S.L., Yee H.K.C., Carlberg R.G., Ellingson E., 1999, *ApJ*, 527, 54
- Bell E.F., De Jong R., 2001, *ApJ*, 550, 212
- Bernardi M. et al., 2002, *AJ*, submitted (astro-ph/0110344)
- Blanton M.R. et al., 2001, *AJ*, 121, 2358
- Blanton M.R. et al., 2002a, *AJ*, submitted (astro-ph/0205243)
- Blanton M.R. et al., 2002b, *ApJ*, submitted (astro-ph/0210215)
- Brinchmann J., Ellis R.S., 2000, *ApJ*, 536, L77
- Bruzual A.G., 1983, *ApJ*, 273, 105
- Bruzual A.G., Charlot S., 1993, *ApJ*, 405, 538
- Bruzual A.G., Charlot S., 2003, *MNRAS*, submitted
- Calzetti D., Kinney A., Storchi-Bergmann T., 1994, *ApJ*, 429, 582
- Cayrel de Strobel G., Hauck B., Francois P., Thevenin F., Friel E., Mermilliod M., Borde S., 1992, *A&AS*, 95, 273
- Charlot S., Fall S.M., 2000, *ApJ*, 539, 718
- Cole S. et al., 2001, *MNRAS*, 326, 255
- Fukugita M., Ichikawa T., Gunn J.E., Doi M., Shimasaku K., Schneider D.P., 1996, *AJ*, 111, 1748
- Gorgas J., Faber S.M., Burstein D., Gonzalez J.J., Courteau S., Proseer C., 1993, *ApJS*, 86, 153
- Gorgas J., Cardiel N., Pedraz S., Gonzalez J.J., 1999, *A&AS*, 139, 29
- Gunn J.E. et al., 1998, *AJ*, 116, 3040
- Hogg D.W., Finkbeiner D.P., Schlegel D.J., Gunn J.E., 2001, *AJ*, 122, 2129
- Jacoby G.H., Hunter D.A., Christian C.A., 1984, *ApJS*, 56, 257
- Kauffmann G., Haehnelt M., 2000, *MNRAS*, 311, 576
- Kauffmann G. et al., 2003, *MNRAS*, 341, 54 (Paper II, this issue)
- Kennicutt R.C., 1983, *ApJ*, 272, 54
- Kroupa P., 2001, *MNRAS*, 322, 231
- Le Borgne J.-F. et al., 2002, (<http://webast.ast.obs-mip.fr/stelib>)
- Liu M.C., Charlot S., Graham J.R., 2000, *ApJ*, 543, 644
- Madau P., Ferguson H.C., Dickinson M.E., Giavalisco M., Steidel C.C., Fruchter A., 1996, *MNRAS*, 283, 1388
- McKay T.A. et al., 2002, *ApJ*, submitted (astro-ph/0108013)
- Pickles A.J., 1998, *PASP*, 110, 863
- Schlegel D.J., Finkbeiner D.P., Davis M., 1998, *ApJ*, 500, 525
- Shimasaku K. et al., 2001, *AJ*, 122, 1238
- Schmidt M., 1968, *ApJ*, 151, 393
- Smith J.A. et al., 2002, *AJ*, 123, 2121
- Stoughton C. et al., 2002, *AJ*, 123, 485
- Strateva I. et al., 2001, *AJ*, 122, 1861
- Strauss M.A. et al., 2002, *AJ*, accepted (astro-ph/0206225)
- Verheijen M.A.W., 2001, *ApJ*, 563, 694
- Wang B., Heckman T.M., 1996, *ApJ*, 457, 645
- Worthey G., Ottaviani D.L., 1997, *ApJS*, 111, 377
- York D.G. et al., 2000, *AJ*, 120, 1579
- Zaritsky D., Smith R., Frenk C.S., White S.D.M., 1993, *ApJ*, 405, 464
- Zaritsky D., Kennicutt R.C., Huchra J.P., 1994, *ApJ*, 420, 47

APPENDIX

Here we describe the mathematical underpinning of the Bayesian likelihood estimates for parameters such as F_{burst} , A_z and M/L that we derive in this paper.

Let us recall the basis of Bayesian statistics for this kind of problem. An initial assumption is made that the data are randomly drawn from a distribution that is a member of a model family characterized by a parameter vector \mathbf{P} . The dimension of \mathbf{P} can, in principle, be arbitrarily large. In particular, it can be much larger than the number of points N in the data set to be fitted. The goal is then to use the data to define a likelihood function on the space of all possible \mathbf{P} . This function can be used to obtain a best estimate and confidence interval for any model property $Y(\mathbf{P})$.

In Bayesian statistics one has to specify a prior distribution on the space of all possible \mathbf{P} . This is a probability density distribution $f_p(\mathbf{P})$, which encodes knowledge concerning the relative likelihood of various \mathbf{P} values in the absence of any data. For example, the physically accessible range for each element of \mathbf{P} may be limited. Typically one takes a uniform prior in parameters with a small dynamic range and a uniform prior in the log of parameters with a large dynamic range.

The likelihood of a particular value of \mathbf{P} given a specific data set \mathbf{d} is then written as a posterior probability density function (using Bayes' theorem) as

$$f(\mathbf{P} | \mathbf{d}) d\mathbf{P} = A f_p(\mathbf{P}) Pr\{\mathbf{d} | \mathbf{P}\} d\mathbf{P}, \quad (\text{A1})$$

where A is a constant that is adjusted so that $f(\mathbf{P} | \mathbf{d})$ normalizes correctly to unity and $Pr\{\mathbf{d} | \mathbf{P}\}$ is the probability of the observed data set on the hypothesis that the underlying distribution is described by the particular parameter set \mathbf{P} .

The likelihood of the derived parameter $Y(\mathbf{P})$ given the data are then

$$f(Y | \mathbf{d}) dY = \int_{\mathbf{P}} f(\mathbf{P} | \mathbf{d}) d\mathbf{P} \quad (\text{A2})$$

where the integral extends over all \mathbf{P} for which Y lies in a specified bin $\pm dY/2$. Note that there is no regularity requirement on the function $Y(\mathbf{P})$ other than piecewise continuity so it makes sense to define a probability density. The most probable value of Y can then be taken as the peak of this distribution; the most typical value as its median; the 95 per cent (symmetric) confidence interval for scalar Y can be defined by excluding the 2.5 per cent tails at each end of the distribution.

When applied to the kinds of problems presented in this paper, the prior is taken to be the distribution of possible star formation histories in the comparison library, which can be viewed as a Monte Carlo sampling of $f_p(\mathbf{P})$. The integral in the above expression for the likelihood of Y is then trivially evaluated through binning the integrand as a function of Y . The expression for $Pr\{\mathbf{d} | \mathbf{P}\}$ is also straightforward for our case, since we have a measure of each element of \mathbf{d} and we can assume the errors are normal with known correlation matrix \mathbf{C} . In this situation

$$Pr\{\mathbf{d} | \mathbf{P}\} \propto \exp \left\{ - [\mathbf{d} - \mathbf{d}_p(\mathbf{P})] \cdot \mathbf{C}^{-1} \cdot [\mathbf{d} - \mathbf{d}_p(\mathbf{P})] / 2 \right\}, \quad (\text{A3})$$

where $\mathbf{d}_p(\mathbf{P})$ is the data vector predicted by the model with parameters \mathbf{P} . The argument of the exponential is then just minus one-half of χ^2 .

It is worth noting that this procedure makes no assumptions concerning the shapes of the distributions $f_p(\mathbf{P})$, $f(\mathbf{P} | \mathbf{d})$ or $f(Y | \mathbf{d})$. The first can be assumed at will, and for small error bars and a well constrained problem should have little effect on the answer. The other two are then derived consistently. The important assumptions are that the model makes a well defined and specific prediction for the value of the observable in the absence of observational errors (in practice there will be some degree of theoretical uncertainty and this could be included in \mathbf{C} if it can be modelled as a Gaussian) and that the observed data \mathbf{d} have a known observational error that can be assumed Gaussian with covariance matrix \mathbf{C} .

This paper has been typeset from a $\text{\TeX}/\text{\LaTeX}$ file prepared by the author.